Space-Time Quantum Metasurfaces

de Melo Kort-Kamp, Wilton Junior
Azad, Abul Kalam
Dalvit, Diego Alejandro Roberto

To be published in: Physical Review Letters

DOI to publisher's version: 10.1103/PhysRevLett.127.043603

Space-Time Quantum Metasurfaces

Wilton J. M. Kort-Kamp,[1] Abul K. Azad,[1] and Diego A. R. Dalvit*[1]

[1]*Los Alamos National Laboratory, Los Alamos, NM 87545, USA*

(Dated: June 4, 2021)

Metasurfaces have recently entered the realm of quantum photonics, enabling manipulation of quantum light using a compact nanophotonic platform. Realizing the full potential of metasurfaces at the deepest quantum level requires the ability to tune coherent light-matter interactions continuously in space and time. Here, we introduce the concept of space-time quantum metasurfaces for arbitrary control of the spectral, spatial, and spin properties of nonclassical light using a compact photonic platform. We show that space-time quantum metasurfaces allow on-demand tailoring of entanglement among all degrees of freedom of a single photon. We also that spatio-temporal modulation induces asymmetry at the fundamental level of quantum fluctuations, resulting in the generation of steered and vortex photon pairs out of vacuum. Space-time quantum metasurfaces have the potential to enable novel photonic functionalities, such as encoding quantum information into high-dimensional color qudits using designer modulation protocols, sculpting multispectral and multispatial modes in spontaneous emission, and generating reconfigurable hyperentanglement for high-capacity quantum communications.

The generation, manipulation, and detection of nonclassical states of light is at the heart of quantum photonics. As quantum information can be encoded into the different degrees of freedom of a single photon, it is highly desirable to develop photonic platforms that allow to control them while maintaining quantum coherence. Metasurfaces [1, 2] have recently transitioned from the classical to the quantum domain [3–16]. Demonstrations of metasurfaces in quantum photonics are based on meta-atoms whose optical properties are determined by their material composition and geometrical design, and the lack of spatio-temporal control severely limits the functionalities that state-of-the-art quantum metasurfaces can attain. At the classical level, space-time metasurfaces have been shown to provide that higher degree of control [17, 18], both by reconfigurable and fully-dynamic tailoring of the optical response of meta-atoms using analog and digital modulation schemes [19, 20]. Transitioning spatio-temporal modulation through the classical-quantum divide could be critical to enable novel opportunities for flat quantum photonics.

Here, we put forward the concept of space-time quantum metasurfaces (STQMs) for spatio-temporal control of quantum light. In the STQM paradigm, meta-atoms are modulated in space and time enabling manipulation of quantum light interacting with the dynamical metasurface. STQMs come in different flavors, including modulated quantum systems such as atomic arrays driven by laser pulses, hybrid quantum-classical systems such as quantum emitters embedded in modulated dielectric nanostructures, and meta-atoms made of classical or quantum materials with driven optical or electro-optical response. In this work we discuss concrete examples for the last two flavors. Figure 1a depicts an all-dielectric STQM for generating multicolor-multipath-spin hyperentanglement on a single photon. Figure 1b illustrates a graphene-based STQM generating vortex dynamical Casimir photons out of the quantum vacuum.

STQM-enabled entanglement manipulation: We first study the entanglement dynamics of a single photon as it transits through a dielectric metasurface whose permittivity is spatio-temporally modulated. The meta-atoms are comprised of high-index dielectrics, that have low optical absorption and result in negligible photon loss. The identical meta-atoms are anisotropic and are suitably rotated with respect to each other (Fig. 1a). The combination of anisotropy and rotation results in circular cross-polarization conversion and a spin-dependent Pancharatnam-Berry geometric phase distribution $\Psi(\mathbf{r})$ akin to spin-orbit coupling [21]. The spatio-temporal modulation is modeled as a harmonic perturbation to the permittivity, $\epsilon(\mathbf{r},t) = \epsilon_{um} + \Delta\epsilon\cos(\Omega t - \Phi(\mathbf{r}))$, where ϵ_{um} is the unmodulated permittivity, $\Delta\epsilon$ the modulation amplitude, Ω the modulation frequency, and $\Phi(\mathbf{r})$ a "synthetic" phase. Such kind of modulation has been recently demonstrated in [22] using an amorphous Si optical metasurface and two slightly detuned near-IR pump beams. Their interference produces a traveling-wave permittivity modulation via the nonlinear Kerr effect in amorphous Si, resulting in $\Phi(\mathbf{r}) = \boldsymbol{\beta}\cdot\mathbf{r}$ and with modulation frequency given by the detuning of the pumps [23]. Note that the geometric phase is fixed by the design of the metasurface, while the modulation momentum "kick" $\boldsymbol{\beta}$ can be reconfigured on-demand.

The geometry of the meta-atoms can be tailored so that their lowest Mie electric and magnetic dipolar resonances dominate the optical response and the STQM has maximal cross-polarized transmission [23]. One can then describe the interaction of each resonator with light using the Hamiltonian $H_{int} = -\mathbf{p}\cdot\mathbf{E} - \mathbf{m}\cdot\mathbf{B}$ [32, 33], where $\mathbf{p}$ and $\mathbf{m}$ are the electric and magnetic dipole operators and $\mathbf{E}$ and $\mathbf{B}$ are the quantized electromagnetic fields. It is convenient to express the Hamiltonian only in terms of photonic modes by relating dipoles and fields via effective electric $\boldsymbol{\alpha}_E$ and magnetic $\boldsymbol{\alpha}_M$ polarizability tensors. Cross-polarized transmission of a normally incident photon can be described via an unmodulated coupling strength $\alpha_{um}^{(cr)}(\omega) = \mathrm{Re}[\alpha_{E,xx}(\omega) + \alpha_{M,yy}(\omega) - \alpha_{E,yy}(\omega) - \alpha_{M,xx}(\omega)]$. Upon spatio-temporal modulation, the polarizabilities adiabatically follow the harmonic driving because the response times of semiconductors are much faster than THz modulations achievable with all-optical schemes.

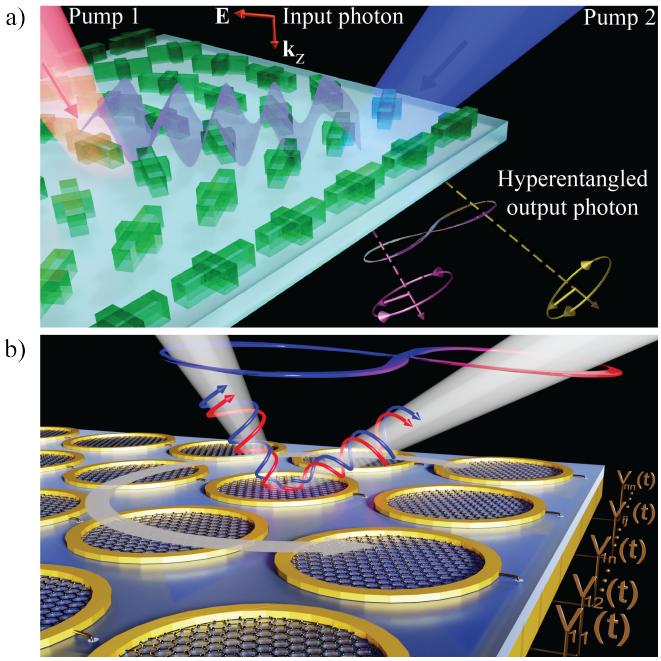

Figure 1. Conceptual representations of space-time quantum metasurfaces. (a) A dielectric STQM with refractive index modulation induces color-spin-path hyperentanglement on a single photon. (b) A graphene-disk STQM with electro-optical modulation generates entangled vortex photon pairs out of the quantum vacuum.

Hence,

$$\alpha^{(cr)}(\omega;\mathbf{r},t)=\alpha^{(cr)}_{um}(\omega)+\Delta\alpha^{(cr)}(\omega)\cos(\Omega t-\Phi(\mathbf{r})). \quad (1)$$

We calculate the polarizability modulation amplitude $\Delta\alpha^{(cr)}(\omega)$ from the dependency of $\alpha^{(cr)}_{um}(\omega)$ on permittivity modulation (Fig. 2a). The STQM Hamiltonian $H_1(t)=-\sum_{j,\gamma,\gamma'}[\alpha^{(cr)}_{um}(\omega)+\Delta\alpha^{(cr)}(\omega)\cos(\Omega t-\Phi_j)]\times A^*_{\gamma;j}A_{\gamma';j}e^{i(\omega-\omega')t}[e^{i\Psi_j}a^\dagger_{\gamma,R}a_{\gamma',L}+e^{-i\Psi_j}a^\dagger_{\gamma,L}a_{\gamma',R}]+h.c.$ results from summing contributions from individual j-th resonators. The STQM annihilates the input photon with frequency ω' and spatial mode $A_{\gamma'}$, and creates a new one with the same or Doppler-shifted frequency, flipped spin components, and added geometric and synthetic phases. Photons are very robust against decoherence in high-index dielectrics, as shown in previous experiments [5]. Temporal fluctuations in the STQM could introduce environmental noise whose quantification depends on the particular modulation protocol. For simplicity, here we consider noise-free modulations and restrict to unitary dynamics.

When the geometric phase is a linear function of the meta-atoms' positions it generates spin-path correlations, while a linear synthetic phase creates path-color correlations. The two correlations are intertwined through path and the photon evolves into a state that is hyperentangled in spin, path, and color [34]

$$|\psi(t)\rangle=\sum_{p,q}c^{(R)}_{p,q}(t)|\omega_p;\mathbf{k}_{p,q};R\rangle+c^{(L)}_{p,q}(t)|\omega_p;\mathbf{k}_{p,-q};L\rangle, \quad (2)$$

where p are integers, $q=0,1$, R (L) denotes right (left) circular polarization, $\omega_p=\omega_{in}+p\Omega$ are harmonics of the input frequency ω_{in}, $\mathbf{k}_{p,q}=\mathbf{k}_{in}+p\boldsymbol{\beta}+q\boldsymbol{\beta}_g$ are momentum harmonics of the in-plane input wave-vector $\mathbf{k}_{in}$, and $\boldsymbol{\beta}_g$ is the momentum kick induced by the geometric phase. Note the STQM makes the photon to occupy high-dimensional color qudit states. We will denote states in the first and second terms of Eq. (2) as (p,q,R) and $(p,-q,L)$, highlighting that the geometric-phase-induced momentum kicks for right- and left-polarized photons have opposite directions. To calculate the probability amplitudes we consider a normally-incident linearly-polarized single-photon pulse and assume $\Omega\ll\omega_{in}$ and $|\boldsymbol{\beta}|,|\boldsymbol{\beta}_g|\ll\omega_{in}/c$. We obtain [23]

$$|c^{(R/L)}_{p,q}(t)|^2=\frac{1}{2}\cos^2\left(\frac{\omega_{in}t\alpha^{(cr)}_{um}}{2hP^2}\right)J^2_p\left(\frac{\omega_{in}t\Delta\alpha^{(cr)}}{2hP^2}\right) \quad (3)$$

when p and q have the same parity; for opposite parity the cosine is replaced by a sine; $J_p(x)$ is the Bessel function. The probability that the output photon is in a given harmonic as a function of the modulation depth is shown in Fig. 2b. At zero modulation, the output has the same frequency as the input and is an equal superposition of right- and left-polarized geometric-phase-kicked states. As the modulation increases, transitions to only the first few frequency/momentum harmonics occur and a larger amount of the Hilbert space is explored at large modulation depths. At oblique incidence, conversion efficiencies into momentum harmonics could deteriorate due to limited performance of phase gradient metasurfaces, and wide-angle metasurfaces could be employed to enhance the transition probabilities [2]. Regarding other input polarization states, the corresponding transition probabilities are calculated in [23]. In particular, circularly-polarized input photons are cross-polarized in transmission and only get color-path entangled at the output.

Figure 2c depicts the density matrix of the input linearly-polarized photon and Figs. 2d-f the output density matrices for different configurations of the STQM: (d) Geometric phase with spatio-temporal modulation off, giving a spin-path entangled output of same frequency as input; (e) No geometric phase and spatio-temporal modulation on, resulting in multicolor-multipath entanglement; (f) Geometric phase with spatio-temporal modulation on, delivering multicolor-multipath-spin hyperentanglement.

We quantify the amount of entanglement using concurrence for qudit multi-partite systems [35, 36]. We obtain $C\approx 0.996$, $C\approx 1.129$, and $C\approx 1.381$ for Figs. 4d,e,f, respectively. Note that the concurrence in these systems is not bound to be less than one. For example, for color-path maximally entangled qudits $C_{max}=\sqrt{2}$, implying that the output state in Fig. 4e is highly entangled. Quantum state tomography or correlation measurements between different degrees of freedom of the output photon could be employed to probe entanglement. Extensions of the above analysis to other geometric and synthetic phase configurations are discussed in [23].

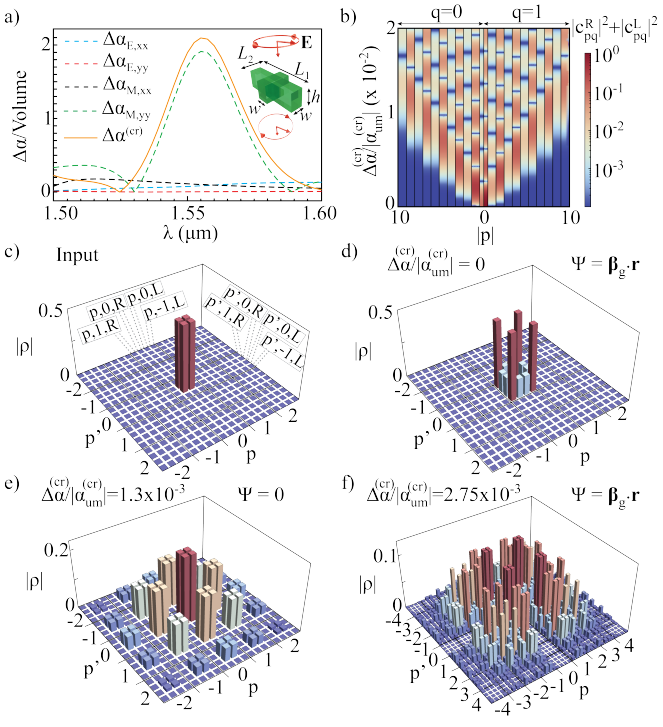

Figure 2. (a) Modulation amplitudes of polarizability tensor components normalized to the meta-atom volume for $\Delta\epsilon/\epsilon_{um} = 1\%$ of an optical all-dielectric STQM designed for maximal cross-polarized transmission at 1550 nm under normal incidence. Inset: Anisotropic amorphous Si meta-atom with $L_1 = 950$ nm, $L_2 = 435$ nm, $h = 300$ nm, $w = 200$ nm, and square unit cell with period $P = 1200$ nm. (b) Conversion probability of a linearly-polarized input photon into an output photon in frequency harmonic $\omega_{in} + p\Omega$ and momentum harmonic $p\boldsymbol{\beta}+q\boldsymbol{\beta}_g$ versus polarizability modulation depth. Density matrices of input (c) and output photons featuring (d) spin-path entanglement, (e) color-path entanglement, and (f) color-spin-path hyperentanglement. Parameters are: $\omega_{in}/2\pi = 193$ THz, $\Omega/2\pi = 10$ THz, $|\boldsymbol{\beta}| = |\boldsymbol{\beta}_g| = 0.01\omega_{in}/c$, 1 ps interaction time, and $\alpha_{um}^{(cr)} = 0.6\mu\text{m}^3$ [23].

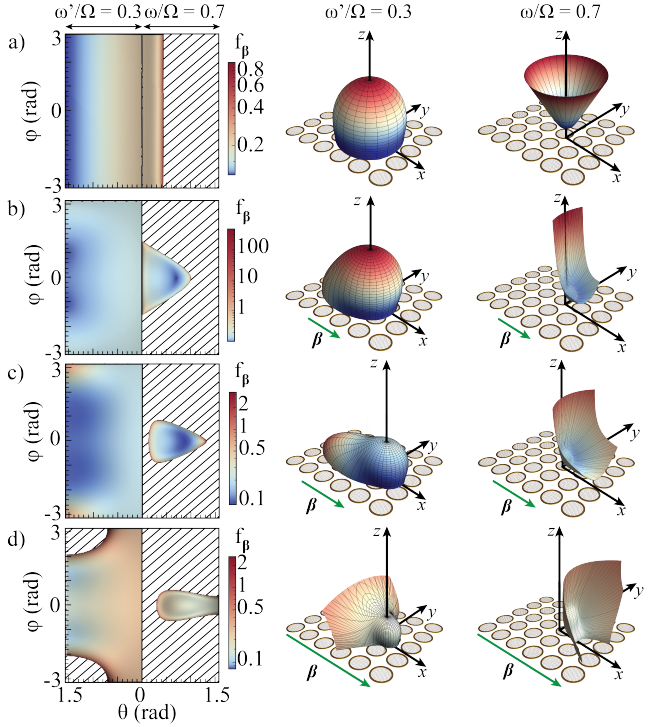

Figure 3. Steered quantum vacuum from a graphene-disk STQM. Density (first column) polar plots of emitted circularly-polarized radiation for various momentum kicks $c\beta/\Omega$ equal to 0 (a), 0.3 (b), 0.38 (c), and 0.5 (d). The areas to the right (left) of the vertical solid line correspond to the emission spectrum of the high- (low-) frequency photon in a pair. The second and third columns show the corresponding spherical polar plots. Parameters are: $\Omega/2\pi = 10$ THz, $\Delta E_F/E_F = 1\%$, $n_{MS} = 10^3$ mm^{-2}, $D = 5$ μm, and $\mu = 10^4$ cm^2 V^{-1} s^{-1}.

STQM-enabled quantum vacuum manipulation: We now study STQMs comprising modulated quantum materials [37] and manipulating quantum vacuum fluctuations. As a simple example, we consider a graphene-disk STQM whose Fermi energy E_F is spatio-temporally modulated, $E_F(\mathbf{r},t) = E_F + \Delta E_F \cos(\Omega t - \Phi(\mathbf{r}))$. The geometric phase is zero and, in the intraband regime, the modulation of E_F results in a corresponding modulation of the electric polarizability of the disks, $\alpha(\omega;\mathbf{r},t) = \alpha_{um}(\omega) + \Delta\alpha(\omega)\cos(\Omega t - \Phi(\mathbf{r}))$. The highly localized plasmons supported by the graphene disks [38–40] result in resonant enhancements of $\Delta\alpha(\omega)$ conducive to efficient coupling of the STQM with the quantum vacuum (inset Fig. 4e). Furthermore, the use of ultra-high mobility graphene minimizes photon absorption [41, 42], which is also desired feature for enhancing the coupling. We design the metasurface to operate in the low-THz regime, and consider modulation frequencies also in the same range, which can be achieved using dynamic optical gratings and graphene's Kerr nonlinearity [23].

The STQM couples to the quantum electromagnetic field via the photon-number-non-conserving Hamiltonian $H_2(t) = (1/8)\sum_{j,\gamma,\gamma'}\sum_{\lambda,\lambda'} [\Delta\alpha(\omega) + \Delta\alpha(\omega')] \times A^*_{\gamma;j}A^*_{\gamma';j}\, e^{i\Phi_j} e^{i(\omega+\omega'-\Omega)t}\, a^\dagger_{\gamma,\lambda}a^\dagger_{\gamma',\lambda'} + h.c.$, where λ, λ' are polarization states of the two photons. This process is essentially an analogue of the dynamical Casimir effect (DCE) in which an oscillating boundary parametrically excites virtual into real photons [43–45]. Interestingly, the STQM synthetic phase allows for a novel degree of control over the quantum vacuum, beyond previously demonstrated analog DCE set-ups [46–49]. Indeed, steered and twisted DCE photons can be produced and the DCE scattering matrix becomes asymmetric [50], reflecting that Lorentz reciprocity is broken at the level of quantum vacuum fluctuations [51].

We compute the rates of photon production out of the quantum vacuum using time-dependent perturbation theory by assuming weak modulation depths of the meta-atoms (other possible approaches are discussed in [44, 45]). Energy conservation dictates that the photon pairs satisfy $\omega + \omega' = \Omega$. The two-photon emission rate from an STQM of area A with arbi-

trary synthetic phase $\Phi(\mathbf{r})$ is

$$\Gamma_\Phi = \frac{An_{MS}^2\Omega^4}{512\pi^3c^4}\int_0^\Omega d\omega|\Delta\alpha(\omega)+\Delta\alpha(\Omega-\omega)|^2 f_\Phi(\omega). \quad (4)$$

The rate scales as the square of the meta-atoms number surface density n_{MS}, indicating coherent emission of photon pairs. The spectral weight function $f_\Phi(\omega)$ results from the integration of all two-photon generation events encoded in the angular emission spectrum. In Figure 3 we show this spectrum $f_\beta(\mathbf{k},\omega)$ for the case of the linear synthetic phase. Momentum conservation enforces that the emitted photons must have in-plane momenta that add up to the imprinted kick, $\mathbf{k}+\mathbf{k}'=\boldsymbol{\beta}$, and the emitted photons are entangled over continuous colors and paths. In the absence of kick the spectra resemble cone- (dome-) like shapes for the high- (low-) frequency photon. As the magnitude of the momentum kick β increases, the emission profiles undergo intricate changes. The directions of allowed emission for the first (second) photon get deformed until at $\beta_{max}=\Omega/c$ they collapse to a single direction and the photon is only emitted parallel (anti-parallel) to the kick. The modulation also excites hybrid entangled pairs composed of one photon and one evanescent surface wave (shaded areas in the left panels), and when $\beta>\beta_{max}$ only evanescent modes are created. The spectral weight function $f_\beta(\omega)$ is plotted in Fig. 4a. At zero kick it has a singular behavior at $\omega/\Omega=0.5$ which results from events where both photons are emitted at grazing angles [52]. For nonzero kick the modulation induces an asymmetry between the photons and such singular events cannot take place. The spectrum develops a central plateau-like form with sharp edges at $\omega_\pm/\Omega=(1\pm c\beta/\Omega)/2$, corresponding to cases where the high (low) frequency photon starts (stops) to be emitted at grazing angles and in azimuthal directions parallel (antiparallel) to the kick.

The STQM can also stir the quantum vacuum and induce angular momentum nonreciprocity [53] that results in entangled vortex-pair generation (Fig. 1b). The required synthetic phase to induce such a process is the spinning phase $\Phi(\mathbf{r})=\ell\varphi$ (ℓ is an arbitrary integer and φ is the azimuthal angle). The modulated metasurface generates photon pairs carrying angular momenta that add up to the imprinted spinning $m+m'=\ell$ in agreement with angular momentum conservation. Photons are color-angular momentum entangled and their correlations could be probed using photo-coincidence detection and techniques based on angular momentum sorting of light [54, 55]. The spectral weight function $f_\ell(\omega)$ is reported in Fig. 4b, showing plateau-like structures with decreasing height as the spinning grows. There is a drastic but subtle difference between $f_\beta(\omega)$ and $f_\ell(\omega)$ that is not apparent in the plots: The former vanishes beyond the finite kick threshold β_{max}, while there is no finite spinning threshold for the latter. Figures 4c-d show the angular momentum spectra of low- and high-frequency photons in an emitted pair. Due to color-angular momentum entanglement and the conservations laws derived above, the probability of emitting a photon with (ω,m) must be the identical to that of creating a photon with $(\Omega-\omega,\ell-m)$. When the STQM does not imprint

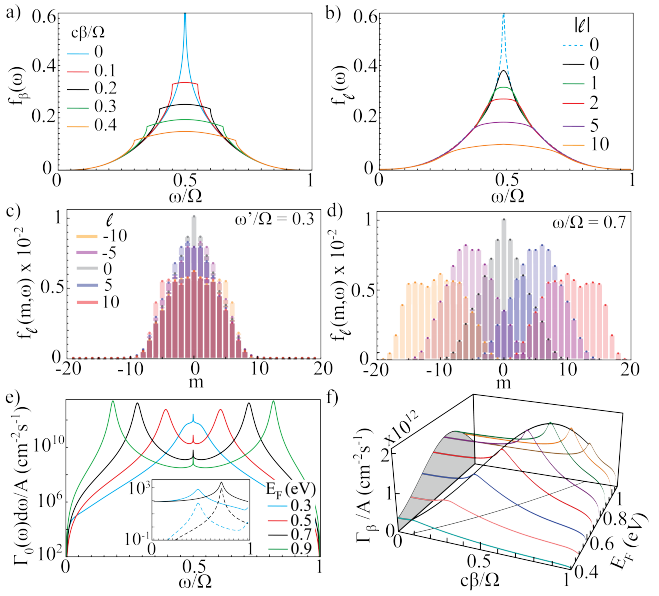

Figure 4. Spectral weight function for (a) linear and (b) rotating synthetic phase. Solid lines in (b) correspond to a finite radius metasurface ($\Omega R/c=30$) and dashed line is the $\ell=0$ case for an infinite metasurface. Angular-momentum spectra for finite radius metasurface for the (c) low- and (d) high-frequency photon. (e) Spectral photo-production rate for null synthetic phase for a graphene-disk STQM. Inset: unmodulated electric polarizability $\alpha_{um}(\omega)$ (solid) and modulation amplitude $\Delta\alpha(\omega)$ (dashed) in units of μm^3. (f) Emission rate for linear synthetic phase. The black thick curve joins peaks of maximal emission and the thin black curve $\omega_{res}(E_F)=(\Omega+c\beta)/2$ is its projection on the $\beta-E_F$ plane. Parameters are the same as in Fig. 3.

any spinning, the spectra are symmetric around the peak at $m=0$, with oppositely twisted photons in each emitted pair. When spinning is present, one intuitively expects that photons will be emitted with the same angular momentum as the drive ($m=\ell$), and because they are created in pairs with complementary angular momentum, emission at $m=0$ should be equally probable, as verified in Figs. 4c,d.

Figure 4e depicts the spectral rate for a STQM for null synthetic phase, featuring Lorentzian peaks at complementary frequencies. For high-Q resonances the emission rate for arbitrary synthetic phase is approximated as

$$\Gamma_\Phi \approx g\Omega\,(An_{MS}^2D^6\omega_{res}^4/c^4)\,f_{\Phi;res}\Big(\frac{\Delta E_F}{E_F}\Big)^2\Big(\frac{\Omega}{\gamma}\Big)^3. \quad (5)$$

Here, $\omega_{res}=(e^2E_F/4\pi^2\varepsilon_0|\xi_1|\hbar^2D)^{1/2}$ is the resonance frequency, D the disk diameter, $f_{\Phi;res}$ the spectral weight on resonance, $\gamma=ev_F^2/E_F\mu$ (Fermi velocity v_F and mobility μ), and $g=5\pi^4a_1^4\xi_1^2/2(512)^3$ is determined by the lowest plasmonic eigenmode coefficients $a_1=6.1$ and $\xi_1=-0.072$. Figure 4f shows the emission rate for the linear synthetic phase as a function of momentum kick and Fermi energy. Giant photon-pair production rates on the order of 10^{12} photons/cm^{2}s are obtained at low-THz driving frequencies and modest modulation depths.

In conclusion, we uncovered a key property of space-time quantum metasurfaces relevant for potential applications: On-demand reconfiguration of the synthetic phase allows dynamically tunable quantum correlations, enabling to tailor the nature of entanglement depending on the symmetry properties of both geometric and synthetic phases. We also illustrated a second key property of space-time quantum metasurfaces with fundamental relevance: Lorentz nonreciprocity at the deepest level of vacuum fluctuations is attained through joint space and time modulations of optical properties and can be interpreted as an asymmetric quantum vacuum. Novel photonic devices potentially enabled by the proposed STQM concept include quantum emitters with reconfigurable spatial modes, quantum nonreciprocal routers and isolators for free-space photon transport in distributed quantum networks, and active quantum sensors with photon steering capabilities to scan a detection area of interest. Beyond solid-state quantum metasurfaces, the extension of the proposed STQM concept to atomic-scale quantum metasurfaces, such as two-dimensional atomic arrays in an optical lattice, could open new paths for manipulating cooperative light-matter interactions at the single-quantum level. As such, space-time quantum metasurfaces can provide breakthrough advances in the broad field of quantum science and technology.

This work was supported by the DARPA QUEST and LANL LDRD programs. We are grateful to A. Efimov, M. Julian, C. Lewis, M. Lucero, and A. Manjavacas for discussions.

*Correspondence: dalvit@lanl.gov

[1] A. V. Kildishev, A. Boltasseva, and V. M. Shalaev, Planar photonics with metasurfaces, Science **339**, 1232009 (2013).

[2] H.-T. Chen, A. J. Taylor, and N. Yu, A review of metasurfaces: physics and applications, Rep. Prog. Phys. **79**, 076401 (2016).

[3] P. K. Jha, X. Ni, C. Wu, Y. Wang, and X. Zhang, Metasurface-Enabled Remote Quantum Interference, Phys. Rev. Lett. **115**, 025501 (2015).

[4] A. S. Solntsev, G. S. Agarwal, and Y. S. Kivshar, Metasurfaces for quantum photonics, arXiv:2007.14722.

[5] T. Stav, A. Faerman, E. Maguid, D. Oren, V. Kleiner, E. Hasman, and M. Segev, Quantum entanglement of the spin and orbital angular momentum of photons using metamaterials, Science **361**, 1101-1104 (2018).

[6] P. K. Jha, N. Shitrit, J. Kim, X.Ren, Y. Wang, and X. Zhang, Metasurface-Mediated Quantum Entanglement, ACS Photonics **5**, 971-976 (2018).

[7] K. Wang, J. G. Titchener, S. S. Kruk, L. Xu, H.-P. Chung, M. Parry, I. I. Kravchenko, Y.-H. Chen, A. S. Solntsev, Y. S. Kivshar, D. N. Neshev, and A. A. Sukhorukov, Quantum metasurface for multiphoton interference and state reconstruction, Science **361**, 1104-1108 (2018).

[8] P. Georgi, M. Massaro, K.-H. Luo, B. Sain, N, Montaut, H. Herrmann, T. Weiss, G. Li, C. Silberhorn, and T. Zentgraf, Metasurface interferometry toward quantum sensors, Light: Science & Applications **8**, 70 (2019).

[9] J. Bohn, T. Bucher, K. E. Chong, A. Komar, D.-Y. Choi, D. N. Neshev, Y. S. Kivshar, T. Pertsch, and I. Staude, Active tuning of spontaneous emission by Mie-resonant dielectric metasurfaces, Nano Lett. **18**, 3461-3465 (2018).

[10] A. Vaskin, R. Kolkowskia, A. F. Koenderink, and I. Staude, Light-emitting metasurfaces, Nanophotonics **8**, 1151-1198 (2019).

[11] Y.-Y. Xie, P.-N. Ni, Q.-H. Wang, Q. Kan, G. Briere, P.-P. Chen, Z.-Z. Zhao, A. Delga, H.-R. Ren, H.-D. Chen, C. Xu, and P. Genevet, Metasurface-integrated vertical cavity surface-emitting lasers for programmable directional lasing emissions, Nat. Nanotech. **15**, 1250-130 (2020).

[12] Y. Kan, S. K. H. Andersen, F. Ding, S. Kumar, C. Zhao, and S. I. Bozhevolnyi, Metasurface-enabled generation of circularly polarized single photons, Adv. Mater. **32**, 1907832 (2020).

[13] L. Li, Z. Liu, X. Ren, S. Wang, V. Su, M.-K. Chen, C. H. Chu, H. Y. Kuo, Bi. Liu, W. Zang, G. Guo, L. Zhang, Z. Wang, S. Zhu, and D. P. Tsai, Metalens-array-based high-dimensional and multiphoton quantum source, Science **368**, 1487-1490 (2020).

[14] Q. Li, W. Bao, Z. Nie, Y. Xia, Y. Xue, Y.Wang, S. Yang, and X. Zhang, A non-unitary metasurface enables continuous control of quantum photon-photon interactions from bosonic to fermionic, Nat. Photonics **15**, 267-271 (2021).

[15] R. Bekenstein, I. Pikovski, H. Pichler, E. Shahmoon, S. F. Yelin, and M. D. Lukin, Quantum metasurfaces with atom arrays, Nat. Phys. **16**, 676-681 (2020).

[16] J. Rui, D. Wei, A. Rubio-Abadal, S. Hollerith, J. Zeiher, D. M. Stamper-Kurn, C. Gross, and I. Bloch, A subradiant optical mirror formed by a single structured atomic layer, Nature **583**, 369-374 (2020).

[17] A. M. Shaltout, V. M. Shalaev, and M. L. Brongersma, Spatiotemporal light control with active metasurfaces, Science **364**, 648 (2019).

[18] C. Caloz and Z.-L. Deck-Léger, Spacetime Metamaterials, IEEE Transactions on Antennas and Propagation **68**, 1569-1582 (2019).

[19] A. E. Cardin, S. R. Silva, S. R. Vardeny, W. J. Padilla, A. Saxena, A. J. Taylor, W. J. M. Kort-Kamp, H.-T. Chen, D. A. R. Dalvit, and A. K. Azad, Surface-wave-assisted nonreciprocity in spatio-temporally modulated metasurfaces, Nat. Commun. **11**, 1469 (2020).

[20] L. Zhang, X. Q. Chen, S. Liu, Q. Zhang, J. Zhao, J. Y. Dai, G. D. Bai, X. Wan, Q. Cheng, G. Castaldi, V. Galdi, and T. J. Cui, Space-time-coding digital metasurfaces, Nat. Commun. **9**, 4334 (2018).

[21] Z. Bomzon, G. Biener, V. Kleiner, and E. Hasman, Space-variant Pancharatnam-Berry phase optical elements with computer-generated subwavelength gratings, Opt. Lett. **27**, 1141-1143 (2002).

[22] X. Guo, Y. Ding, Y. Duan, and X. Ni, Nonreciprocal metasurface with space-time phase modulation, Light: Science & Applications **8**, 123 (2019).

[23] See Supplementary Information, that contains references [24–31].

[24] A. B. Evlyukhin, C. Reinhardt, E. Evlyukhin, and B. N. Chichkov, Multipole analysis of light scattering by arbitrary-shaped nanoparticles on a plane surface, J. Opt. Soc. Am. B **30**, 2589 (2013).

[25] H. J. Eichler, P. Günter, and D. H. Pohl, *Laser induced dynamical gratings* (Springer-Verlag, Heidelberg, 1986).

[26] D. Naidoo, K. Ait-Ameur, M. Brunel, and A. Forbes, Intracavity generation of superpositions of Laguerre-Gaussian beams, Appl. Phys. B, **106**, 683-690 (2012).

[27] G. F. Calvo, A. Picón, and E. Bagan, Quantum field theory of photons with orbital angular momentum, Phys. Rev. A **73**, 013805 (2006).

[28] J. L. Cheng, N. Vermeulen and J. E. Sipe, Third-order nonlinearity of graphene: Effects of phenomenological relaxation and finite temperature, Phys. Rev. B **91**, 235320 (2015).

[29] S. A. Mikhailov, Quantum theory of the third-order nonlinear electrodynamic effects of graphene, Phys. Rev. B **93**, 085403 (2016).

[30] C. L. Holloway, M. A. Mohamed, E. F. Kuester, and A. Dienstfrey, Reflection and transmission properties of a metafilm: with an application to a controllable surface composed of resonant particles, IEEE Transactions on Electromagnetic Compatibility **47**, 853-865 (2005).

[31] S. J. Van Enk and G. Nienhuis, Commutation rules and eigenvalues of spin and orbital angular momentum of radiation fields, J. Mod. Opt. **41**, 963-977 (1994).

[32] A. I. Kuznetsov, A. E. Miroshnichenko, M. L. Brongersma, Y. S Kivshar, and B. Luk'yanchuk, Optically resonant dielectric nanostructures, Science **354**, aag2472 (2016).

[33] L. Novotny and B. Hecht, *Principles of Nano-Optics* (Cambridge University Press, New York, 2007).

[34] J. T. Barreiro, N. K. Langford, N. A. Peters, and P. G. Kwiat, Generation of Hyperentangled Photons Pairs, Phys. Rev. Lett. **95**, 260501 (2005).

[35] P. Rungta, V. Buzek, C. M. Caves, M. Hillery, and G. J. Milburn, Universal state inversion and concurrence in arbitrary dimensions, Phys. Rev. A **64**, 042315 (2001).

[36] F. Mintert, A. R. R. Carvalho, M. KuÅ>, and A. Buchleitner, Measures and dynamics of entangled states, Phys. Reports **415**, 207-259 (2005).

[37] B. Keimer and J. E. Moore, The physics of quantum materials, Nat. Phys. **13**, 1045-1055 (2017).

[38] R. Yu, J. D. Cox, J. R. M. Saavedra, and F. J. García de Abajo, Analytical modeling of graphene plasmons, ACS Photonics **4**, 3106 (2017).

[39] F. J. García de Abajo and A. Manjavacas, Plasmonics in atomically thin materials, Faraday Discuss. **178**, 87-1073548 (2015).

[40] Y. Muniz, A. Manjavacas, C. Farina, D. A. R. Dalvit, and W. J. M. Kort-Kamp, Two-Photon Spontaneous Emission in Atomically Thin Plasmonic Nanostructures, Phys. Rev. Lett. **125**, 033601 (2020).

[41] K. I. Bolotin, K. J. Sikes, Z. Jiang, M. Klima, G. Fudenberg, J. Hone, P. Kim, and H. L. Stormer, Ultrahigh electron mobility in suspended graphene, Solid State Commun. **146**, 351-355 (2008).

[42] C. R. Dean, A. F. Young, I. Meric, C. Lee, L. Wang, S. Sorgenfrei, K. Watanabe, T. Taniguchi, P. Kim, K. L. Shepard, and J. Hone, Boron nitride substrates for high-quality graphene electronics, Nat. Nanotechnol. **5**, 722-726 (2010).

[43] G. T. Moore, Quantum theory of the electromagnetic field in a variable-length one-dimensional cavity, Journal of Mathematical Physics **11**, 2679 (1970).

[44] D. A. R. Dalvit, P. A. Maia Neto, and F. D. Mazzitelli, in Casimir Physics, Lecture Notes in Physics **834** (eds. D. Dalvit, P. Milonni, D. Roberts, and F. Da Rosa), (Springer, Heidelberg, 2006).

[45] V. V. Dodonov, Current status of the dynamical Casimir effect, Physica Scripta **82**, 038105 (2010).

[46] C. M. Wilson, G. Johansson, A. Pourkabirian, M. Simoen, J. R. Johansson, T. Duty, F. Nori, and P. Delsing, Observation of the dynamical Casimir effect in a superconducting circuit, Nature **479**, 376-379 (2011).

[47] J.-C. Jaskula, G. B. Partridge, M. Bonneau, R. Lopes, J. Ruaudel, D. Boiron, and C. I. Westbrook, Acoustic Analog to the Dynamical Casimir Effect in a Bose-Einstein Condensate, Phys. Rev. Lett. **109**, 220401 (2012).

[48] P. Lahteenmaki, G. S. Paraoanu, J. Hassel, and P. J. Hakonen, Dynamical Casimir effect in a Josephson metamaterial, Proc. Nat. Acad. Sci. USA **110**, 4234-4238 (2013).

[49] S. Vezzoli, A. Mussot, N. Westerberg, A. Kudlinski, H. D. Saleh, A. Prain, F. Biancalana, E. Lantz, and D. Faccio, Optical analogue of the dynamical Casimir effect in a dispersion-oscillating fibre, Commun. Phys. **2**, 84 (2019).

[50] M. F. Maghrebi, R. Golestanian, and M. Kardar, Scattering approach to the dynamical Casimir effect, Phys. Rev. D **87**, 025016 (2013).

[51] D. L. Sounas and A. Alù, Non-reciprocal photonics based on time modulation, Nat. Photonics **1**, 774-783 (2017).

[52] P. A. Maia Neto and L. A. S. Machado, Quantum radiation generated by a moving mirror in free space, Phys. Rev. A **54**, 3420 (1996).

[53] D. L. Sounas, C. Caloz, and A. Alù, Giant non-reciprocity at the subwavelength scale using angular momentum-biased metamaterials, Nat. Commun. **4**, 2407 (2013).

[54] G. C. Berkhout, M. P. Lavery, J. Courtial, M. W. Beijersbergen, and M. J. Padgett, Efficient Sorting of Orbital Angular Momentum States of Light, Phys. Rev. Lett. **105**, 153601 (2010).

[55] M. Mirhosseini, M. Malik, Z. Shi, and R. W. Boyd, Efficient separation of the orbital angular momentum eigenstates of light, Nat. Commun. **4**, 2783 (2013).

Supplementary Information for: Space-Time Quantum Metasurfaces

Wilton J. M. Kort-Kamp, Abul K. Azad, and Diego A. R. Dalvit
Los Alamos National Laboratory, Los Alamos, NM 87545, USA

I. EFFECTIVE POLARIZABILITIES AND HAMILTONIAN FOR ALL-DIELECTRIC STQM

The unit cell design of the anisotropic dielectric meta-atom is shown in Supplementary Figure 1a (the same structure is shown in the main Fig. 2a). We calculate via full-wave simulations the transmission and reflection spectra of the periodic metasurface for a normally-incident plane-wave (Supplementary Figure 1b), showing high cross-polarized transmission. We perform a Cartesian multipole expansion [1] of the obtained polarization field $\mathbf{P}(\mathbf{R},\omega) = \epsilon_0(\epsilon(\omega) - 1)\mathbf{E}(\mathbf{R},\omega)$, where $\epsilon(\omega)$ is the electric permittivity of the meta-atoms and $\mathbf{E}$ is the total local electric field. The associated electric and magnetic Mie dipoles are

$$\begin{aligned}\mathbf{p}(\omega) &= \int d\mathbf{R}'\, \mathbf{P}(\mathbf{R}',\omega),\\ \mathbf{m}(\omega) &= -\frac{i\omega}{2}\int d\mathbf{R}'\, [\mathbf{R}'\times\mathbf{P}(\mathbf{R}',\omega)],\end{aligned} \tag{S1}$$

where the integrals are over the volume of any given meta-atom. We obtain effective electric $\boldsymbol{\alpha}_E(\omega)$ and magnetic $\boldsymbol{\alpha}_M(\omega)$ polarizability tensors for the meta-atom by writing the dipoles in terms of the incident plane-wave evaluated at the center $\mathbf{R}_0$ of the dielectric resonator, $\mathbf{p}(\omega) = \epsilon_0\boldsymbol{\alpha}_E(\omega)\mathbf{E}_{inc}(\mathbf{R}_0,\omega)$ and $\mathbf{m}(\omega) = \mu_0^{-1}\boldsymbol{\alpha}_M(\omega)\mathbf{B}_{inc}(\mathbf{R}_0,\omega)$. The corresponding polarizability modulation tensors $\Delta\boldsymbol{\alpha}_E(\omega)$ are shown in Supplementary Figure 1c, and the field distribution for the corresponding dipolar electric and magnetic resonances are shown in Supplementary Figure 1d. The modulated polarizabilities $\Delta\boldsymbol{\alpha}_{E/M}(\omega)$ are calculated by analyzing the change of $\boldsymbol{\alpha}_E(\omega)$ and $\boldsymbol{\alpha}_M(\omega)$ when $\epsilon(\omega)$ is varied around a chosen working point $\epsilon_{um}(\omega)$. The results for the modulated polarizabilities are reported in Fig. 2a of the main text, and repeated here in Supplementary Figure 1e for completeness.

In-plane rotation of each anisotropic $j-$th meta-atom around its center $\mathbf{R}_{0;j} = (\mathbf{r}_j, z_j)$ by an angle θ_j results in a rotated polarizability tensor. In the $(\mathbf{e}_L, \mathbf{e}_R, \mathbf{z})$ basis (left and right circular polarization unit vectors $\mathbf{e}_{L/R} = (\mathbf{x} \pm i\mathbf{y})/\sqrt{2}$) it reads

$$\boldsymbol{\alpha}_{E/M;j} = R(\theta_j)\boldsymbol{\alpha}_{E/M}R(-\theta_j) = \begin{pmatrix} \frac{1}{2}(\alpha_{E/M,xx}+\alpha_{E/M,yy}) & \frac{1}{2}e^{-i\Psi_j}(\alpha_{E/M,xx}-\alpha_{E/M,yy}) & 0\\ \frac{1}{2}e^{i\Psi_j}(\alpha_{E/M,xx}-\alpha_{E/M,yy}) & \frac{1}{2}(\alpha_{E/M,xx}+\alpha_{E/M,yy}) & 0\\ 0 & 0 & \alpha_{E/M,zz}\end{pmatrix}, \tag{S2}$$

where $R(\theta_j)$ is the rotation matrix and $\Psi_j = -2\theta_j$ is the geometric phase distribution induced by rotation. Anisotropy $\alpha_{E/M,xx} \neq \alpha_{E/M,yy}$ and rotation generate spin-orbit coupling contained in the off-diagonal components.

The Hamiltonian describing the interaction of the quantum electromagnetic field with the geometric phase STQM is $H_{int}(t) = -\sum_j \mathbf{p}_j(t)\cdot\mathbf{E}(\mathbf{r}_j,z_j,t) - \sum_j \mathbf{m}_j(t)\cdot\mathbf{B}(\mathbf{r}_j,z_j,t)$. Here $\mathbf{p}_j$ and $\mathbf{m}_j$ are electric and magnetic dipole operators associated to each meta-atom and $\mathbf{E}$ and $\mathbf{B}$ are field operators. We assume the STQM is free-standing and its permittivity is modulated as $\epsilon(\omega;\mathbf{r},t) = \epsilon_{um}(\omega) + \Delta\epsilon(\omega)\cos(\Omega t - \Phi(\mathbf{r}))$, where $\Phi(\mathbf{r})$ is the synthetic phase. Dipole and field operators are related as

$$\mathbf{d}_j(\omega) = \epsilon_0\boldsymbol{\alpha}_{E;j}(\omega)\mathbf{E}(\mathbf{r}_j,z_j,\omega) + \frac{1}{2}e^{-i\Phi_j}\epsilon_0\Delta\boldsymbol{\alpha}_{E;j}(\omega+\Omega)\mathbf{E}(\mathbf{r}_j,z_j,\omega+\Omega) + \frac{1}{2}e^{i\Phi_j}\epsilon_0\Delta\boldsymbol{\alpha}_{E;j}(\omega-\Omega)\mathbf{E}(\mathbf{r}_j,z_j,\omega-\Omega) \tag{S3}$$

and similarly for $\mathbf{m}_j(\omega)$. Relevant frequencies are around the input photon frequency ω_{in} and, in the approximation $\Omega \ll \omega_{in}$, we neglect Doppler shifts in the polarizabilities in Eq. (S3) but keep them in the fields to account for frequency harmonic generation. $H_{int}(t)$ can be expressed as a sum of four terms: co-polarized transmission and reflection containing in-plane diagonal components in Eq. (S2), and cross-polarized transmission and reflection with the non-diagonal components. For a normally-incident photon and in the quasi-paraxial approximation, the corresponding unmodulated effective coupling strengths are

$$\begin{aligned}\alpha_{um;t}^{(co/cr)}(\omega) &= \mathrm{Re}[\alpha_{E,xx}(\omega)+\alpha_{M,yy}(\omega)] \pm \mathrm{Re}[\alpha_{E,yy}(\omega)+\alpha_{M,xx}(\omega)],\\ \alpha_{um;r}^{(co/cr)}(\omega) &= \mathrm{Re}[\alpha_{E,xx}(\omega)-\alpha_{M,yy}(\omega)] \pm \mathrm{Re}[\alpha_{E,yy}(\omega)-\alpha_{M,xx}(\omega)],\end{aligned} \tag{S4}$$

the plus (minus) sign associated with co- (cross-) polarization. The same relations hold for the corresponding effective polarizability modulation amplitudes $\Delta\alpha_{t/r}^{(co/cr)}(\omega)$. We work in the regime when the cross-polarized coupling strength

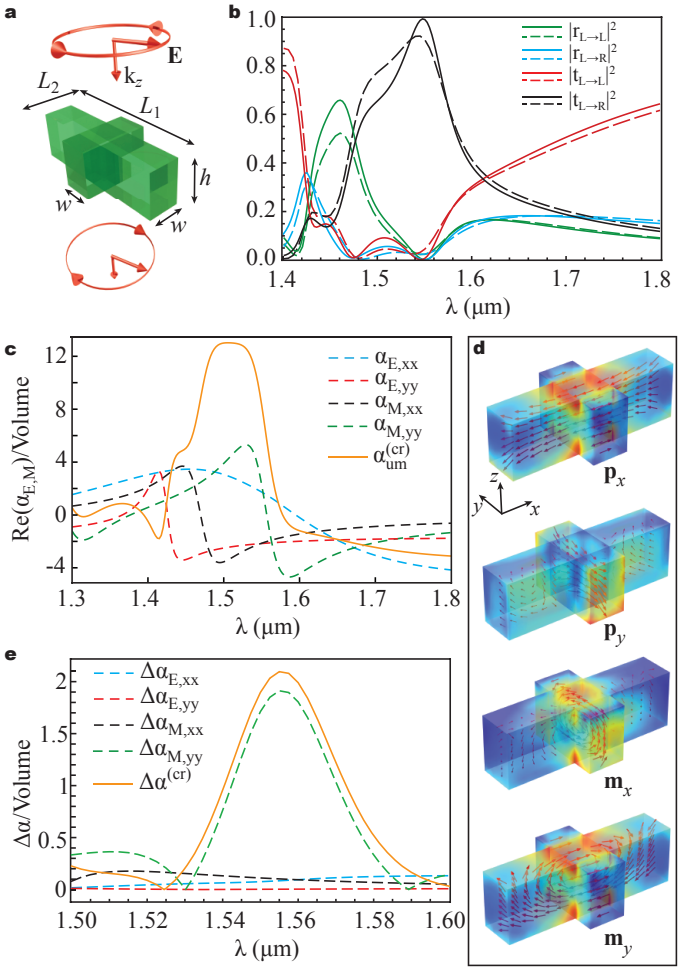

FIG. S1. Effective polarizabilities of all-dielectric space-time quantum metasurfaces. (a) Anisotropic amorphous Si Mie nanocross meta-atom with optimized geometrical parameters for maximal cross-polarization transmission for a normally-incident $\lambda_{in} = 1550$ nm input photon. Parameters are $L_1 = 950$ nm, $L_2 = 435$ nm, $h = 300$ nm, $w = 200$ nm, and square unit cell with period $P = 1200$ nm. (b) Co- and cross-polarized reflectivity and transmissivity for the full metasurface (solid) and electric/magnetic dipole array (dashed). (c) Real parts of the electric and magnetic polarizabilities normalized by the meta-atom volume. Solid line is the effective unmodulated coupling strength for cross-polarized transmission: $\alpha_{um}^{(cr)} \approx 0.6\mu\text{m}^3$ at the input frequency. (d) Electric field distribution for the two electric and the two magnetic Mie resonances. (e) Polarizability modulation amplitudes for permittivity modulation depth $\Delta\epsilon/\epsilon_{um} = 1\%$. Solid line is the polarizability modulation amplitude for cross-polarized transmission: $\Delta\alpha^{(cr)}/\alpha_{um}^{(cr)} \approx 16\%$ at the input frequency.

in transmission is much larger than the other three and we approximate the total Hamiltonian by its cross-polarized transmission part (henceforth we omit the subscript t in $\Delta\alpha_t^{(cr)}(\omega)$). The photon-number-conserving part of the Hamiltonian is

$$H_1(t) = -\sum_{j,\gamma,\gamma'} A^*_{\gamma;j} A_{\gamma';j} e^{i(\omega-\omega')t} \left[\alpha_{um}^{(cr)}(\omega) + \Delta\alpha^{(cr)}(\omega)\cos(\Omega t - \Phi_j)\right] \left[e^{i\Psi_j} a^\dagger_{\gamma,R} a_{\gamma',L} + e^{-i\Psi_j} a^\dagger_{\gamma,L} a_{\gamma',R}\right] + h.c. \quad \text{(S5)}$$

The sums are over all meta-atoms and field modes, $a_{\gamma',L/R}$ is an annihilation operator of a left/right circular polarized photon, and $a^\dagger_{\gamma,R/L}$ is a creation operator of a right/left polarized photon, and $A_{\gamma;j}$, $A_{\gamma';j}$ are spatial modes. The process of two-photon emission from dielectric STQMs, also contained in the full Hamiltonian, is less efficient than in all-plasmonic ultra-thin STQMs because these enable giant modulation amplitudes.

All-optical modulation schemes of an amorphous Si STQM can be employed to get high modulation frequencies. For example, to obtain a linear synthetic phase one can implement a laser-induced dynamical optical grating through the interference of two slightly detuned, non-collinear Gaussian laser beams [2]. A Ti:Sapphire laser (800 nm central wavelength, 20 nm bandwidth, peak intensity $I_P = 15$ GW cm^{-2}) can be split into two beams using a beam splitter,

each part is then detuned to $\lambda_{P1} = 2\pi c/\omega_{P1} = 810$ nm and $\lambda_{P2} = 2\pi c/\omega_{P2} = 790$ nm using tunable optical parametric amplifiers (OPAs), and then they are made to interfere on the amorphous Si metasurface to generate an optical dynamical grating with intensity proportional to $I_P \cos(\Omega t - \beta x)$. The modulation frequency is equal to the detuning, $\Omega = \omega_{P1} - \omega_{P2} = 2\pi \times 10$ THz, and the modulation wavevector β is equal to the difference of the in-plane wavevectors of the pumps that can be controlled by the angles of incidence of the pumps. Due to the nonlinear optical Kerr effect of amorphous Si, the moving optical grating induces a traveling-wave modulation of its effective linear permittivity of the form $\epsilon(\omega; \mathbf{r}, t) = \epsilon_{um}(\omega) + \Delta\epsilon(\omega)\cos(\Omega t - \boldsymbol{\beta}\cdot\mathbf{r})$ with the modulation amplitude being proportional to the third-order susceptibility $\chi^{(3)}(\omega, \omega_{P1}, -\omega_{P2})$. Permittivity modulation depths of the order of 1% can be achieved. As shown in Fig. S1, this leads to a 16% polarizability modulation depth. The increase is due to the strong dispersion of the unmodulated polarizability around the input frequency. Such a rotating synthetic phase could be implemented, e.g., via a heterodyne laser-induced dynamical grating with Laguerre-Gauss petal modes [3, 4] to generate an all-optical spinning perturbation of the meta-atoms' refractive index

II. INTERACTION HAMILTONIANS FOR VARIOUS SYNTHETIC AND GEOMETRIC PHASES IN ALL-DIELECTRIC STQMS

When both the synthetic and geometric phase distributions are linear, $\Phi(\mathbf{r}) = \boldsymbol{\beta}\cdot\mathbf{r}$ and $\Psi(\mathbf{r}) = \boldsymbol{\beta}_g\cdot\mathbf{r}$, we quantize the electromagnetic field using modes labelled by $\gamma = \{\mathbf{k}, \zeta, \omega\}$ and plane-wave (PW) spatial mode functions $A_\gamma^{(PW)}(\mathbf{r}, z) = (\hbar\omega/2V)^{1/2} e^{i(\mathbf{k}\cdot\mathbf{r} + \zeta|k_z|z)}$. Here, $\zeta = \pm$ corresponds to upward ($k_z > 0$) or downward ($k_z < 0$) propagation, respectively. $V = NhP^2$ is the quantization volume, N the number of meta-atoms, h the height of the meta-atom, and P the size of the square unit cell. Meta-atoms are located at $z_j = 0$. The quasi-paraxial approximation requires momentum kicks much smaller than the input wave-vector, $|\boldsymbol{\beta}|, |\boldsymbol{\beta}_g| \ll \omega_{in}/c$. Then

$$H_1^{(\boldsymbol{\beta},\boldsymbol{\beta}_g)}(t) = -\sum_j \sum_{\mathbf{k},\zeta,\omega} \sum_{\mathbf{k}',\zeta',\omega'} \frac{\hbar\sqrt{\omega\omega'}}{4V} [\alpha_{um}^{(cr)}(\omega) + \Delta\alpha^{(cr)}(\omega)\cos(\Omega t - \boldsymbol{\beta}\cdot\mathbf{r}_j)] e^{i(\omega-\omega')t} \times \delta_{\zeta,\zeta'}\, e^{-i(\mathbf{k}-\mathbf{k}')\cdot\mathbf{r}_j} [e^{i\boldsymbol{\beta}_g\cdot\mathbf{r}_j} a^\dagger_{\mathbf{k},\zeta,\omega,R}\, a_{\mathbf{k}',\zeta',\omega',L} + e^{-i\boldsymbol{\beta}_g\cdot\mathbf{r}_j} a^\dagger_{\mathbf{k},\zeta,\omega,L}\, a_{\mathbf{k}',\zeta',\omega',R}] + h.c. \tag{S6}$$

where we use that in transmission $\zeta = \zeta'$. The superscript in H_1 highlights the type of synthetic and geometric phases. This STQM Hamiltonian generates frequency-spin-path hyperentanglement.

A similar Hamiltonian can be written when the synthetic and geometric phases are both spinning distributions, $\Phi(\mathbf{r}) = \ell\varphi$ and $\Psi(\mathbf{r}) = \ell_g\varphi$. As there is no in-plane momentum kick, the paraxial approximation is exact for a normally-incident photon. We employ paraxial quantization of the electromagnetic field with orbital angular momentum (OAM) [5]. Modes are labelled by $\gamma = \{l, p, \zeta, \omega\}$ and spatial mode functions are Laguerre-Gauss (LG), $A_\gamma^{(LG)}(\rho, \varphi, z) = (\hbar\omega/2V)^{1/2} LG_{l,p,\zeta,\omega}(\rho, \varphi, z)$. l is the winding number and p the number of modal nodes in the radial direction. Then,

$$H_1^{(\ell,\ell_g)}(t) = -\sum_j \sum_{l,p,\zeta,\omega} \sum_{l',p',\zeta',\omega'} \frac{\hbar\sqrt{\omega\omega'}}{4V} [\alpha_{um}^{(cr)}(\omega) + \Delta\alpha^{(cr)}(\omega)\cos(\Omega t - \ell\varphi_j)] e^{i(\omega-\omega')t}$$
$$\times\delta_{\zeta,\zeta'} LG^*_{l,n,\zeta,\omega}(\rho_j, \varphi_j, -ct) LG_{l',p',\zeta',\omega'}(\rho_j, \varphi_j, -ct) \Big[e^{i\ell_g\varphi_j} a^\dagger_{l,p,\zeta,\omega,R}\, a_{l',p',\zeta',\omega',L} + e^{-i\ell_g\varphi_j} a^\dagger_{l,p,\zeta,\omega,L}\, a_{l',p',\zeta',\omega',R} \Big] + h.c. \tag{S7}$$

We use standard notation of LG beams for which the coordinate system is attached to the beam center at $z = 0$. This Hamiltonian generates frequency-OAM-spin hyperentanglement.

For mixed-phase STQMs, e.g., $\Phi(\mathbf{r}) = \boldsymbol{\beta}\cdot\mathbf{r}$ and $\Psi(\mathbf{r}) = \ell_g\varphi$, we express the linear synthetic phase in the cylindrical basis appropriate for the geometric phase. Using $\exp(i\boldsymbol{\beta}\cdot\mathbf{r}) = \sum_{n=0}^{\infty} i^n J_n(\beta\rho) e^{in\varphi}$, with $\beta = |\boldsymbol{\beta}|$, and assume small in-plane kicks for paraxial quantization with LG modes. The Hamiltonian is

$$H_1^{(\boldsymbol{\beta},\ell_g)}(t) = -\sum_j \sum_{l,p,\zeta,\omega} \sum_{l',p',\zeta',\omega'} \frac{\hbar\sqrt{\omega\omega'}}{4V} \Big\{ \alpha_{um}^{(cr)}(\omega) + \frac{1}{2}\Delta\alpha^{(cr)}(\omega) \sum_n i^n J_n(\beta\rho_j) \Big[e^{i(\Omega t - n\varphi_j)} + (-1)^n e^{-i(\Omega t - n\varphi_j)} \Big] \Big\} e^{i(\omega-\omega')t}$$
$$\times\delta_{\zeta,\zeta'} LG^*_{l,p,\zeta,\omega}(\rho_j, \varphi_j, -ct)\; LG_{l',p',\zeta',\omega'}(\rho_j, \varphi_j, -ct) \Big[e^{i\ell_g\varphi_j} a^\dagger_{l,p,\zeta,\omega,R}\, a_{l',p',\zeta',\omega',L} + e^{-i\ell_g\varphi_j} a^\dagger_{l,p,\zeta,\omega,L}\, a_{l',p',\zeta',\omega',R} \Big] + h.c. \tag{S8}$$

Importantly, this mixed-phase Hamiltonian does not generate hyperentanglement but only bi-partite OAM-spin entanglement in the LG basis. Alternatively, one can expand the spinning geometric phase in terms of plane-waves and employ plane-wave quantization. The transformed Hamiltonian generates the same output state, which is now frequency-path entangled in the PW basis. The evolved state can then be written in either basis as

$$|\psi^{(\boldsymbol{\beta},\ell_g)}(t)\rangle = \sum_{p\geq 0} A_p^{(\ell_g)}(t) \left[|\omega_p; \mathbf{k}_{p,0}\rangle + |\omega_{-p}; \mathbf{k}_{-p,0}\rangle \right] \otimes |\lambda_{in}\rangle = \sum_p \sum_{q=0,1} B_{pq}^{(\boldsymbol{\beta})}(t) |\omega_p\rangle \otimes \left[|\ell_{0,q}; R\rangle + |\ell_{0,-q}; L\rangle \right], \tag{S9}$$

where $\omega_p = \omega_{in} + p\Omega$, $\mathbf{k}_{p,q} = \mathbf{k}_{in} + p\boldsymbol{\beta} + q\boldsymbol{\beta}_g$, $\ell_{p,q} = p\ell + q\ell_g$, and $|\lambda_{in}\rangle$ is the input linearly polarized state. The Hamiltonian $H_1^{(\ell,\boldsymbol{\beta}_g)}(t)$ can be similarly derived.

III. ENTANGLEMENT DYNAMICS IN STQMS

We compute the evolution operator $U^{(\Phi,\Psi)}(t) = \mathcal{T}\exp[-(i/\hbar)\int_0^t dt' H_1(t')]$ under the time-dependent STQM Hamiltonian $H_1(t)$ in Eq. (S5), with Φ and Ψ arbitrary synthetic and geometric phases ($\mathcal{T}$ denotes time-ordering). We re-write the spin-dependent part of the Hamiltonian in terms of Pauli matrices as $e^{i\Psi}|R\rangle\langle L| + e^{-i\Psi}|L\rangle\langle R| = e^{i\sigma_3\Psi}\sigma_1$ and expand the evolution operator in its Dyson series. Terms in the series with even powers of H_1 allow to group the factors $e^{i\sigma_3\Psi}\sigma_1$ in pairs and then their product is equal to the identity because $e^{i\sigma_3\Psi}\sigma_1 e^{i\sigma_3\Psi}\sigma_1 = e^{i\sigma_3\Psi}\sigma_1^2 e^{-i\sigma_3\Psi} = \mathbb{I}$ per the anti-commutation relations of Pauli matrices. Terms of the series with odd powers of the Hamiltonian allow to group all factors by pairs except one, and their product is then equal to the ungrouped factor. Therefore,

$$U^{(\Phi,\Psi)}(t) = U_{even}^{(\Phi)}(t)\otimes\mathbb{I} + U_{odd}^{(\Phi)}(t)\otimes e^{i\sigma_3\Psi}\sigma_1. \tag{S10}$$

As a result, geometric-phase-induced momentum kicks $\pm q\hbar\nabla\Psi$ and angular momenta $\pm q\hbar\ell_g$ have $q = 0, 1$ as the only possible values. Expressions for $U_{even}^{(\Phi)}(t)$ and $U_{odd}^{(\Phi)}(t)$ depend on the specifics of the synthetic phase. The output photon state from the metasurface is $|\psi_{out}\rangle = U^{(\Phi,\Psi)}(t_{int})|\psi_{in}\rangle$, where t_{int} is the photon-STQM effective interaction time.

We now consider linear geometric/synthetic phases and an input photon $|\psi_{in}\rangle = |\omega_{in};\mathbf{k}_{in};\lambda_{in}\rangle$ in polarization state $|\lambda_{in}\rangle = \lambda_{in}^{(R)}|R\rangle + \lambda_{in}^{(L)}|L\rangle$. Then

$$U^{(\boldsymbol{\beta},\boldsymbol{\beta}_g)}(t)|\psi_{in}\rangle = \sum_p\Big(\tilde{c}_{p,0}(t)|\omega_p;\mathbf{k}_{p,0}\rangle\otimes[\lambda_{in}^{(R)}|R\rangle + \lambda_{in}^{(L)}|L\rangle]\Big) + \sum_p\Big(\tilde{c}_{p,1}(t)[\lambda_{in}^{(R)}|\omega_p;\mathbf{k}_{p,-1};L\rangle + \lambda_{in}^{(L)}|\omega_p;\mathbf{k}_{p,1};R\rangle]\Big). \tag{S11}$$

The first term produces frequency-path entanglement and the second frequency-spin-path hyperentanglement. Defining $c_{p,0}^{(R/L)}(t) = \lambda_{in}^{(R/L)}\tilde{c}_{p,0}(t)$ and $c_{p,1}^{(R/L)}(t) = \lambda_{in}^{(L/R)}\tilde{c}_{p,1}(t)$ we re-write

$$|\psi(t)\rangle = \sum_{p,q}[c_{p,q}^{(R)}(t)|\omega_p;\mathbf{k}_{p,q};R\rangle + c_{p,q}^{(L)}(t)|\omega_p;\mathbf{k}_{p,-q};L\rangle]. \tag{S12}$$

where we recall that $q = 0, 1$ and p is an integer. The probability amplitudes satisfy coupled-mode equations that follow from Schrödinger equation

$$\begin{aligned}
\dot{c}_{p,0}^{(R/L)} &= i\omega_p\,\eta_{um}\,c_{p,1}^{(L/R)} + i(\omega_p\omega_{p+1})^{1/2}\,\eta\,c_{p+1,1}^{(L/R)} + i(\omega_p\omega_{p-1})^{1/2}\,\eta\,c_{p-1,1}^{(L/R)},\\
\dot{c}_{p,1}^{(R/L)} &= i\omega_p\eta_{um}\,c_{p,0}^{(L/R)} + i(\omega_p\omega_{p+1})^{1/2}\,\eta\,c_{p+1,0}^{(L/R)} + i(\omega_p\omega_{p-1})^{1/2}\,\eta\,c_{p-1,0}^{(L/R)},
\end{aligned} \tag{S13}$$

with initial conditions $c_{p,0}^{(R/L)}(0) = \lambda_{in}^{(R/L)}\delta_{p,0}$ and $c_{p,1}^{(R/L)}(0) = 0$. Here, $\eta_{um} = \alpha_{um}^{(cr)}/2hP^2$ and $\eta = \Delta\alpha^{(cr)}/4hP^2$. We solve the modes equations in the limit $|\boldsymbol{\beta}|, |\boldsymbol{\beta}_g| \ll \omega_{in}/c$ and consider only the lowest diffraction orders. This means that the output paths are quasi-paraxial with the input path. Furthermore, we also assume $\Omega \ll \omega_{in}$ and approximate all square roots by ω_{in}. Using the generating function approach we find

$$\begin{aligned}
c_{p,0}^{(R/L)}(t) &= \frac{1}{2}i^p\lambda_{in}^{(R/L)}J_p(2\eta\omega_{in}t)\left[e^{i\eta_{um}\omega_{in}t} + (-1)^p e^{-i\eta_{um}\omega_{in}t}\right],\\
c_{p,1}^{(R/L)}(t) &= \frac{1}{2}i^p\lambda_{in}^{(L/R)}J_p(2\eta\omega_{in}t)\left[e^{i\eta_{um}\omega_{in}t} - (-1)^p e^{-i\eta_{um}\omega_{in}t}\right],
\end{aligned} \tag{S14}$$

For a linearly-polarized input and p and q of the same parity, the probabilities are $|c_{pq}^{(R)}(t)|^2 = |c_{pq}^{(L)}(t)|^2 = (1/2)\cos^2(\eta_{um}\omega_{in}t)J_p^2(2\eta\omega_{in}t)$ and for opposite parity the cosine is replaced by a sine. Because the modulation is harmonic, the probabilities are invariant under the exchange $p \leftrightarrow -p$. Note that within the quasi-paraxial and small-frequency modulation limits, $c_{p,q}^{(R/L)}(t)$ do not explicitly depend on Ω, $\boldsymbol{\beta}$ or $\boldsymbol{\beta}_g$. However, these parameters do enter into the labeling of the conversion states (p, q, R) and $(p, -q, L)$ through the frequency harmonics $\omega_p = \omega_{in} + p\Omega$ and momentum harmonics $\mathbf{k}_{p,q} = p\boldsymbol{\beta} + q\boldsymbol{\beta}_g$. When the modulation is off ($\eta = 0$), the photon undergoes Rabi oscillations between states $q = 0$ and $q = 1$ suffering linear kicks $\pm\boldsymbol{\beta}_g$ and conserving its input frequency, and the output state is path-spin entangled. When the modulation is on ($\eta \neq 0$), Rabi oscillations are still present, frequency-conversion takes place, and the state is hyperentangled in frequency-spin-path. When the modulation is

only temporal ($\boldsymbol{\beta}=0$), the index p corresponds only to frequency harmonic as there is no synthetic phase momentum kick, and the evolution equations are still given by Eq. (S14).

When the STQM design does not have a geometric phase ($\Psi=0$), the evolution operator is $U^{(\Phi,0)}(t)=\tilde{U}^{(\Phi)}_{even}(t)\otimes\mathbb{I}+\tilde{U}^{(\Phi)}_{odd}(t)\otimes\sigma_1$. For the linear synthetic phase

$$U^{(\boldsymbol{\beta},0)}(t)|\psi_{in}\rangle=\sum_p|\omega_p;\mathbf{k}_{p,0}\rangle\otimes\Big([\lambda^{(R)}_{in}\tilde{c}_{p,0}(t)+\lambda^{(L)}_{in}\tilde{d}_{p,0}(t)]|R\rangle+[\lambda^{(L)}_{in}\tilde{c}_{p,0}(t)+\lambda^{(R)}_{in}\tilde{d}_{p,0}(t)]|L\rangle\Big). \tag{S15}$$

Frequency-path entanglement is generated and no Rabi oscillations are present as the $q=1$ state does not exist. The probability amplitudes $d^{(R)}_p(t)=\lambda^{(R)}_{in}\tilde{c}_{p,0}(t)+\lambda^{(L)}_{in}\tilde{d}_{p,0}(t)$ and $d^{(L)}_p(t)=\lambda^{(L)}_{in}\tilde{c}_{p,0}(t)+\lambda^{(R)}_{in}\tilde{d}_{p,0}(t)$ for right and left polarizations have initial conditions $d^{(R/L)}_p(0)=\lambda^{(R/L)}_{in}\delta_{p,0}$, and satisfy the following coupled-mode equation with the quoted solution

$$\begin{aligned}\dot{d}^{(R/L)}_p&=i\omega_p\eta_{um}\;d^{(L/R)}_p+i(\omega_p\omega_{p+1})^{1/2}\;\eta\;d^{(L/R)}_{p+1}+i(\omega_p\omega_{p-1})^{1/2}\;\eta\;d^{(L/R)}_{p-1},\\ d^{(R/L)}_p(t)&=\frac{1}{2}(-1)^pJ_p(2\eta\omega_{in}t)[(\lambda^{(R)}_{in}+\lambda^{(L)}_{in})e^{i\eta_{um}\;\omega_{in}t}\pm(\lambda^{(R)}_{in}-\lambda^{(L)}_{in})e^{-i\eta_{um}\;\omega_{in}t}],\end{aligned} \tag{S16}$$

where we used $p\Omega\ll\omega_{in}$ to get the solution in the second line. For a linearly-polarized input, the right and left probabilities are the same $|d^{(R)}_p(t)|^2=|d^{(L)}_p(t)|^2=(1/2)J^2_p(2\eta\omega_{in}t)$. Supplementary Figure 2 shows the population dynamics of the in-transit photon, both in the presence and absence of a linear geometric phase.

We quantify entanglement using concurrence generalized to qudit bi-partite [6] and multi-partite [7] systems. For bi-partite systems with dimensions d_1 and d_2, the generalization is the I-concurrence given by $C=\sqrt{2(1-Tr(\rho^2_r))}$, where ρ_r is the reduced density matrix. Maximally-entangled states have $C_{max}=\sqrt{2(1-1/min(d_1,d_2))}$. For N-partite systems ($N>2$), the generalization is $C=2^{1-\frac{N}{2}}\sqrt{(2^N-2)-\sum_i Tr(\rho^2_{r,i})}$, where the summation is over the 2^N-2 non-trivial partitions of the N-partite system. We note that a single scalar measure cannot fully characterize the correlations present in multi-partite systems. For example, for the prototypical maximally entangled three qubit GHZ and W states, $|GHZ\rangle=(1/\sqrt{2})(|111\rangle+|000\rangle)$ and $|W\rangle=(1/\sqrt{3})(|100\rangle+|010\rangle+|001\rangle)$, the generalized concurrence takes different values, $C=\sqrt{3/2}$ and $C=\sqrt{4/3}$, respectively.

For an STQM with geometric phase and modulation off, bi-partite spin-path entanglement is generated. The spin degree of freedom (DOF) has $d_1=2$, the path DOF has $d_2=3$, and the concurrence of the output state is

$$C_{spin-path}=\sqrt{2-2\sum_q\Big(|c^{(R)}_{0q}|^4+|c^{(L)}_{0q}|^4+2|c^{(R)}_{0q}|^2|c^{(L)}_{0q}|^2\Big)}. \tag{S17}$$

$C_{max}=1$ in this case. For the state of Fig. 2d in the main text we obtain $C\approx0.996$, which is very close to the maximum value indicating highly efficient entanglement generation. The output state is not maximally entangled because the photon has a small but non-zero probability of exiting the STQM unsteered ($|c^{(R/L)}_{00}|^2\neq0$). For an STQM without geometric phase and modulation on, bi-partite color-path entanglement is generated. In this case, $d_1=d_2=\infty$ because both the color and path DOF take infinite countable values corresponding to infinite number of harmonics. The concurrence reads

$$C_{color-path}=\sqrt{2-2\sum_p\Big(|d^{(R)}_p|^4+|d^{(L)}_p|^4+2|d^{(R)}_p|^2|d^{(L)}_p|^2\Big)} \tag{S18}$$

$C_{max}=\sqrt{2}$ in this case. For the state in Fig. 2e we obtain $C\approx1.129$, and hence $C/C_{max}\approx0.8$. Finally, in the presence of geometric phase and modulation on, spin-color-path hyperentanglement is generated by the STQM. In this case $N=3$ and $d_1=2$, $d_2=d_3=\infty$. Concurrence takes the form

$$C_{color-spin-path}=\frac{1}{\sqrt{2}}\sqrt{6-\sum_{i=1}^{6}Tr(\rho^2_i)}. \tag{S19}$$

The full density matrix is $\rho=|\psi(t)\rangle\langle\psi(t)|$ and the various reduced density matrices are defined by tracing over degrees of freedom as follows: $\rho_1=Tr_{spin}(\rho)$, $\rho_2=Tr_{color}(\rho)$, $\rho_3=Tr_{path}(\rho)$, $\rho_4=Tr_{color-spin}(\rho)$ $\rho_5=Tr_{spin-path}(\rho)$,

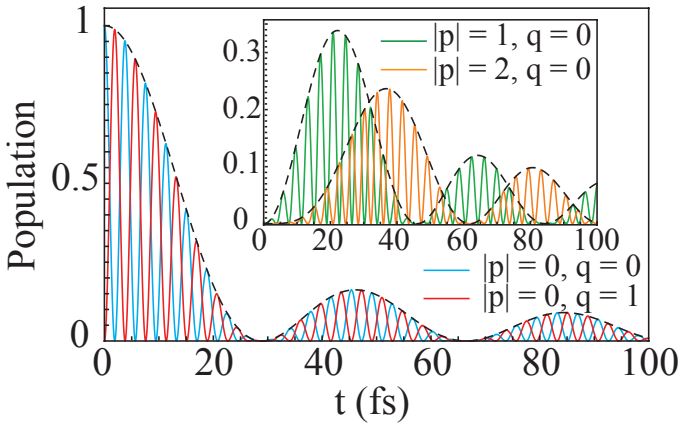

FIG. S2. Population dynamics of geometric-phase kicked $q = 1$ and unkicked $q = 0$ states for in-transit photon, showing Rabi oscillations for the fundamental frequency harmonic. Inset: Rabi dynamics in higher harmonics. Envelopes (dashed black) are the populations of p-harmonics in the absence of geometric phase. The input photon is linearly-polarized and impinges at normal incidence on the STQM. Parameters are: $\omega_{in}/2\pi = 193$ THz, $\Omega/2\pi = 10$ THz, $|\boldsymbol{\beta}| = |\boldsymbol{\beta}_g| = 0.01\omega_{in}/c$, $\alpha_{um}^{(cr)} = 0.6\mu\text{m}^3$, and $\Delta\alpha/\alpha_{um}^{(cr)} = 0.1$. Geometrical parameters of the metasurface as the same as in Fig. S1.

$\rho_6 = Tr_{color-path}(\rho)$. To evaluate the purities it is convenient to slightly change notation and let the index q run from -1 to 1, $|\psi(t)\rangle = \sum_p \sum_{q=-1}^{1} \sum_{s=R,L} c_{p,q}^{(s)}(t)|\omega_p; \mathbf{k}_{p,q}; s\rangle$, with $c_{p,-1}^{(R)}(t) = c_{p,1}^{(L)}(t) = 0$. Then,

$$
\begin{aligned}
Tr(\rho_1^2) = Tr(\rho_6^2) &= \sum_{p,p'}\sum_{q,q'}\sum_{s,s'} c_{p,q}^{(s)} c_{p',q'}^{*(s)} c_{p',q'}^{(s')} c_{p,q}^{*(s')} = \Big(\sum_{p,q} |c_{p,q}^{(R)}|^2\Big)^2 + \Big(\sum_{p,q} |c_{p,q}^{(L)}|^2\Big)^2 + 2\Big|\sum_{p} c_{p,0}^{(R)} c_{p,0}^{*(L)}\Big|^2 \\
Tr(\rho_2^2) = Tr(\rho_5^2) &= \sum_{p}\sum_{q,q'}\sum_{s,s'} |c_{p,q}^{(s)}|^2 |c_{p,q'}^{*(s')}|^2 = \sum_{p}\Big[\Big(\sum_{q} |c_{pq}^{(R)}|^2\Big)^2 + \Big(\sum_{q} |c_{pq}^{(L)}|^2\Big)^2 + 2\Big(\sum_{q} |c_{pq}^{(R)}|^2\Big)\Big(\sum_{q} |c_{pq}^{(L)}|^2\Big)\Big] \\
Tr(\rho_3^2) = Tr(\rho_4^2) &= \sum_{p}\sum_{q,q'}\sum_{s,s'} c_{p,q}^{(s)} c_{p,q}^{*(s')} c_{p,q'}^{(s')} c_{p,q'}^{*(s)} = \sum_{p}\Big[\Big(\sum_{q} |c_{pq}^{(R)}|^2\Big)^2 + \Big(\sum_{q} |c_{pq}^{(L)}|^2\Big)^2 + 2\Big|c_{p0}^{(R)} c_{p0}^{*(L)}\Big|^2\Big]
\end{aligned}
\tag{S20}
$$

For Fig. 4f we obtain $C \approx 1.381$. To the best of our knowledge, a value for C_{max} in the general multi-partite case is not available.

IV. ALL-OPTICAL MODULATION OF GRAPHENE STQM

Here we describe the all-optical modulation scheme of the graphene STQM using the nonlinear optical Kerr effect. In the intraband regime $\omega < 2E_F$, the zero-temperature linear conductivity of graphene takes the Drude form $\sigma_{xx}^{(1)}(\omega) = \sigma_{yy}^{(1)}(\omega) = ie^2E_F/\pi\hbar^2(\omega + i\gamma)$, where E_F is the Fermi energy, $\gamma = ev_F^2/E_F\mu$ is the scattering rate, v_F is the Fermi velocity, and μ is the mobility of graphene. Due to the inversion symmetry of its crystal structure, pristine graphene has no second-order nonlinear conductivity. The real part of the third-order conductivity leads to saturable absorption and the imaginary part to the optical Kerr effect, i.e., the nonlinear phase shift of the refractive index. The third-order nonlinear conductivity tensor $\sigma_{ijkl}^{(3)}(\omega_1, \omega_2, \omega_3)$ has eight non-zero components but just three are independent [8, 9]. At zero temperature and for intraband transitions ($\omega_1, \omega_2, \omega_3 < 2E_F$),

$$
\sigma_{xxxx}^{(3)}(\omega_1, \omega_2, \omega_3) = \sigma_{yyyy}^{(3)}(\omega_1, \omega_2, \omega_3) = \frac{ie^2}{4\pi\hbar^2}\frac{(v_F e)^2}{6E_F(\omega_1 + i\gamma)(\omega_2 + i\gamma)(\omega_3 + i\gamma)} \tag{S21}
$$

and all other components $\sigma_{xxyy}^{(3)} = \sigma_{yyxx}^{(3)}$, $\sigma_{xyxy}^{(3)} = \sigma_{yxyx}^{(3)}$ and $\sigma_{xyyx}^{(3)} = \sigma_{yxxy}^{(3)}$ are given by the same expresssion.

To generate a traveling-wave modulation, we consider a pair of x-polarized plane waves of frequencies ω_{P1} and ω_{P2} (detuning $\Omega = \omega_{P1} - \omega_{P2} > 0$), equal intensity $I_P = (1/2)c\epsilon_0|E_P|^2$, impinging on graphene at angles of incidence θ_{P1} and θ_{P2}: $\mathbf{E}_{P1}(\mathbf{r}, z, t) = \hat{\mathbf{x}}E_P e^{i(\omega_{P1}t - (\omega_{P1}/c)sin\theta_{P1}y - k_{z,P1}z)} + c.c.$ and $\mathbf{E}_{P2}(\mathbf{r}, z, t) = \hat{\mathbf{x}}E_P e^{i(\omega_{P2}t - (\omega_{P2}/c)sin\theta_{P2}y - k_{z,P2}z)} + c.c.$. Their interference on the metasurface plane ($z = 0$) creates a dynamical optical grating with an intensity profile proportional to $\cos(\Omega t - \beta_y y)$, where $\beta_y = (\omega_{P1}/c)\sin\theta_{P1} - (\omega_{P2}/c)\sin\theta_{P2}$. A probe field $\mathbf{E}(\mathbf{r}, z, t) = \mathbf{E}e^{i(\omega t - \mathbf{k}\cdot\mathbf{r} - k_z z)} + c.c.$ impinges on graphene under the above modulation. To first-order in the conductivity, the current generated on

graphene that oscillates with the probe frequency is $J_x^{(1)}(\mathbf{r},t) = E_x\sigma_{xx}^{(1)}(\omega)e^{i(\omega t-\mathbf{k}\cdot\mathbf{r})} + c.c.$. The part of the third-order current that gives the nonlinear Kerr effect oscillating at the probe frequency is contained in $\sigma_{xxxx}^{(3)}(\omega,\omega_{P1},-\omega_{P2})$ and $\sigma_{xxxx}^{(3)}(\omega,-\omega_{P1},\omega_{P2})$, giving

$$\begin{aligned} J_x^{(3)}(\mathbf{r},t) &= \int_{-\infty}^{\infty} d\omega_1 d\omega_2 d\omega_3 E_x(\omega_1)E_x(\omega_2)E_x(\omega_3)\sigma_{xxxx}^{(3)}(\omega_1,\omega_2,\omega_3)e^{i\ (\omega_1+\omega_2+\omega_3)t} \\ &= 12\cos(\Omega t-\beta_y y)\sigma_{xxxx}^{(3)}(\omega,\omega_{P1},-\omega_{P2})E_x|E_P|^2e^{i(\omega t-\mathbf{k}\cdot\mathbf{r})} + c.c. \end{aligned} \tag{S22}$$

We can then define an effective spatio-temporally modulated conductivity

$$\sigma_{xx}^{eff}(\omega;y,t) = \sigma_{yy}^{eff}(\omega;y,t) = \frac{ie^2}{\pi\hbar^2(\omega+i\gamma)}\left[E_F - \frac{4\pi\ \hbar\alpha_{fs}v_F^2 I_P}{E_F\omega_{P1}\omega_{P2}}\cos(\Omega t-\beta_y y)\right], \tag{S23}$$

where α_{fs} is the fine structure constant. The same result is obtained for the effective spatio-temporally modulated conductivity $\sigma_{yy}^{eff} = \sigma_{xx}^{eff}$ because $\sigma_{yyxx}^{(3)} = \sigma_{xxxx}^{(3)}$. The off-diagonal terms are zero, $\sigma_{xy}^{eff} = \sigma_{yx}^{eff} = 0$, because $\sigma_{xy}^{(1)} = \sigma_{yx}^{(1)} = \sigma_{xyxx}^{(3)} = \sigma_{xyyx}^{(3)} = 0$. The above result implies that the Fermi energy is effectively modulated as $E_F(y,t) = E_F + \Delta E_F\cos(\Omega t-\beta_y y)$ with a modulation depth

$$\frac{\Delta E_F}{E_F} = \frac{4\pi\hbar\alpha_{fs}v_F^2 I_P}{E_F^2\omega_{P1}\omega_{P2}}. \tag{S24}$$

A possible implementation of this scheme can be achieved by splitting a 800 nm pulse from a Ti:Sapphire laser into two beams and pass them through optical parametric amplifiers (OPAs) to down-convert them to mid-IR, for example $\omega_{P1}/2\pi = 30$ THz ($\lambda_{P1} = 10\mu$m) and $\omega_{P2}/2\pi = 20$ THz ($\lambda_{P2} = 15\mu$m). The intraband condition is satisfied for $E_F > 0.1$ eV, which can be implemented by electrical doping. The modulation frequency is 10 THz. We estimated the value of the Fermi energy modulation depth using experimentally feasible parameters. For example, for $E_F = 0.3$ eV and $I_P = 0.01$ GW cm^{-2}, the modulation depth is $\approx 1\%$, which is the value used in Figs. 3 and 4 of the main text. Note the required intensity is much lower than in the case of amorphous Si ($I_P \sim 10$'s GW cm^{-2}) thanks to the giant nonlinearity of graphene.

V. ELECTRIC POLARIZABILITIES OF ALL-PLASMONIC STQMS

We employ the plasmon wave-function formalism [10] to compute the electric polarizability tensors of ultra-thin plasmonic meta-atoms. For the disk geometry the geometric phase is zero due to rotational symmetry, and the unmodulated electric polarizability is $\boldsymbol{\alpha}_E(\omega) = \alpha_{um}(\omega)\ \mathrm{diag}(1,1,0)$, where

$$\alpha_{um}(\omega) = \frac{\pi^3 D^3}{128}\sum_{n=1}^{\infty}\frac{a_n^2}{1/\xi_{um}(\omega)-1/\xi_n}, \tag{S25}$$

where the sum is over the bright-mode plasmonic eigenmodes of the disk [11]. Here, D is the disk diameter, $n-1$ denotes the number of nodes along the radial direction, a_n are dimensionless coefficients related to the mode eigenvector, $\xi_n < 0$ is the mode eigenvalue, and $\xi_{um}(\omega) = i\sigma(\omega)/4\pi\epsilon_0\hbar\omega D$ contains the electro-optical properties of graphene. We describe graphene's conductivity $\sigma(\omega)$ via a Drude model at zero temperature and neglect inter-band transitions, i.e., $\sigma(\omega) = ie^2E_F/\pi\hbar^2(\omega+i\gamma)$, where E_F is the Fermi energy, $\gamma = ev_F^2/E_F\mu$ is the scattering rate, v_F is the Fermi velocity, and μ is the mobility of graphene. The unmodulated polarizability has localized plasmonic resonances at

$$\omega_{res;n} = \Big(\frac{\alpha_{fs}cE_F}{\pi|\xi_n|\hbar D}\Big)^{1/2}, \tag{S26}$$

where α_{fs} is the fine structure constant.

We assume a spatio-temporal modulation of the Fermi energy of graphene disks of the form $E_{F;j}(t) = E_F + \Delta E_F\cos(\Omega t-\Phi_j)$, where E_F is the Fermi energy working level and ΔE_F is the modulation amplitude. For small Fermi energy modulation depths we approximate $\alpha_j(\omega;t) \approx \alpha_{um}(\omega) + \Delta\alpha(\omega)\cos(\Omega t-\Phi_j)$, where the polarizability modulation amplitude results

$$\Delta\alpha(\omega) = \frac{\pi^3 D^3}{128}\frac{\Delta E_F}{E_F}\xi_{um}(\omega)\sum_{n=1}^{\infty}\frac{a_n^2\xi_n^2}{[\xi_n-\xi_{um}(\omega)]^2}. \tag{S27}$$

We choose to tailor the disk diameter and the Fermi energy so that the first bright-mode plasmonic resonance of the disk $\omega_{res;n=1}$ is within the DCE spectrum and all other higher-order bright-modes have resonant frequencies larger than Ω ($a_1 = 6.1$ and $\xi_1 = -0.072$ for the $n = 1$ mode [11]). When the resonance has a high-Q ($\gamma/\Omega \ll 1$) the polarizabilities are well-approximated as

$$\alpha_{um}(\Omega u) \approx i\frac{\pi^3 D^3}{256}\Big(\frac{\pi a_1|\xi_1|\alpha_{fs}cE_F}{D\hbar\Omega^2}\Big)^{1/2}\frac{(\gamma/2\Omega)}{(u-u_{res})^2+(\gamma/2\Omega)^2},$$
$$\Delta\alpha(\Omega u) \approx \frac{\pi^2 a_1^2\alpha_{fs}cD^2\Delta E_F}{512\hbar\Omega^2}\frac{(\gamma/2\Omega)^2}{[(u-u_{res})^2+(\gamma/2\Omega)^2]^2}, \tag{S28}$$

where $u = \omega/\Omega$ and $u_{res} = \omega_{res;n=1}/\Omega$.

We gauge the impact of multiscattering among the all-plasmonic STQM meta-atoms using the approach based on effective surface polarizabilities in [12]. Multi-scattering can be neglected when $P \gg \alpha_{um}^{1/3}$ at resonance, where P is the size of the square unit cell of the metasurface. This is approximately satisfied for the parameters used in the main paper and we therefore consider all graphene disks to be non-interacting.

VI. TWO-PHOTON EMISSION FROM STQMS WITH LINEAR SYNTHETIC PHASE

For the array of all-plasmonic two-dimensional isotropic meta-atoms we describe their interaction with the quantum electromagnetic field via the electric dipole Hamiltonian $H_{int}(t) = -\sum_j \mathbf{p}_j(t)\cdot\mathbf{E}(\mathbf{r}_j, z_j, t)$ and write the dipoles in terms of the field using the corresponding polarizabilities. Photon emission arises solely from the modulated part of the Doppler shifted electric dipole operator (Eq. (S3)). Discarding counter-rotating contributions, the Hamiltonian is

$$H_2(t) = \frac{1}{8}\sum_{j,\gamma,\gamma'}\sum_{\lambda,\lambda'}[\Delta\alpha(\omega)+\Delta\alpha(\omega')]e^{i\Phi_j}e^{i(\omega+\omega'-\Omega)t}A^*_{\gamma;j}A^*_{\gamma';j}\,a^\dagger_{\gamma,\lambda}a^\dagger_{\gamma',\lambda'} + h.c. \tag{S29}$$

In contrast to what is done for the problem of the single photon interacting with the STQM (Eq. (S5)), here one must maintain the Doppler shift in the polarizability modulation amplitude because photons are emitted over the broad DCE spectral range from $\omega = 0$ to $\omega = \Omega$. Also, as photons are emitted in arbitrary directions, non-paraxial quantization is required. The probability amplitude of generating a photon-pair is computed with first-order time-dependent perturbation theory and the energy conservation relation $\omega + \omega' = \Omega$ is obtained.

For the linear synthetic phase (Supplementary Figure 3a) we use plane-wave modes which directly allow for non-paraxial quantization. The probability density rate of emitting the photon pair irrespective of the polarization of one of the photons is

$$\mathcal{P}_{\boldsymbol{\beta}}(\mathbf{k},\omega;\mathbf{k}',\omega') = \frac{\Omega^2 N^2}{1024(2\pi)^5}\,\delta(\omega+\omega'-\Omega)\,|\Delta\alpha(\omega)+\Delta\alpha(\omega')|^2\,\mathcal{R}_{\boldsymbol{\beta}}(\mathbf{k},\omega;\mathbf{k}',\omega'),$$

$$\mathcal{R}_{\boldsymbol{\beta}}(\mathbf{k},\omega;\mathbf{k}',\omega') = \frac{\omega\omega'}{\Omega^2N^2|\mathbf{k}|^2|\mathbf{k}'|^2}\Big\{(\mathbf{k}\cdot\mathbf{k}')^2\Big[1+\Big(\frac{c^2k_zk_z'}{\omega\omega'}\Big)^2\Big]+|(\mathbf{k}\times\mathbf{k}')|^2\Big[\Big(\frac{ck_z}{\omega}\Big)^2+\Big(\frac{ck_z'}{\omega'}\Big)^2\Big]\Big\}\,\Big|\sum_j e^{-i(\mathbf{k}+\mathbf{k}'-\boldsymbol{\beta})\cdot\mathbf{r}_j}\Big|^2. \tag{S30}$$

with $k_z^2 = \omega^2/c^2 - |\mathbf{k}|^2 > 0$ and $(k_z')^2 = (\omega')^2/c^2 - |\mathbf{k}'|^2 > 0$. The summation above gives the in-plane momentum conservation relation $\mathbf{k}+\mathbf{k}' = \boldsymbol{\beta}$. In Supplementary Figure 3b we show the one-photon angular emission distribution for a fixed propagation direction of its twin, indicating how the externally imprinted momentum controls the directivity of the emission process. The spectral photon emission rates per unit area for photons with right or left polarization, in-plane momentum in the interval $(\mathbf{k}, \mathbf{k}+d\mathbf{k})$ and frequency in the interval $(\omega, \omega+d\omega)$ is

$$\frac{d\Gamma^{(R/L)}_{\boldsymbol{\beta}}(\mathbf{k},\omega)}{d\mathbf{k}d\omega} = \frac{\omega}{c^2k_z}\,\frac{An_{MS}^2\Omega^2}{512(2\pi)^3c}\,|\Delta\alpha(\omega)+\Delta\alpha(\Omega-\omega)|^2\,f_{\boldsymbol{\beta}}(\mathbf{k},\omega),$$

$$f_{\boldsymbol{\beta}}(\mathbf{k},\omega) = \frac{\omega(\Omega-\omega)^2}{c\Omega^2|\mathbf{k}|^2|\boldsymbol{\beta}-\mathbf{k}|^2k_z'}\left[(\mathbf{k}\cdot(\boldsymbol{\beta}-\mathbf{k}))^2\left(1+\frac{c^4k_z^2(k_z')^2}{\omega^2(\Omega-\omega)^2}\right)+|\mathbf{k}\times\boldsymbol{\beta}|^2\left(\frac{c^2k_z^2}{\omega^2}+\frac{c^2(k_z')^2}{(\Omega-\omega)^2}\right)\right]. \tag{S31}$$

In Supplementary Figure 3c we plot $f_{\boldsymbol{\beta}}(\mathbf{k},\omega)$ for the high-frequency ($\omega > \Omega/2$) and low-frequency ($\omega' < \Omega/2$) photons in the emitted pair. In the absence of kick, the high-frequency photon can be emitted in any azimuthal direction but it has a maximum polar angle of emission, while no such a constraint exists for the low-frequency

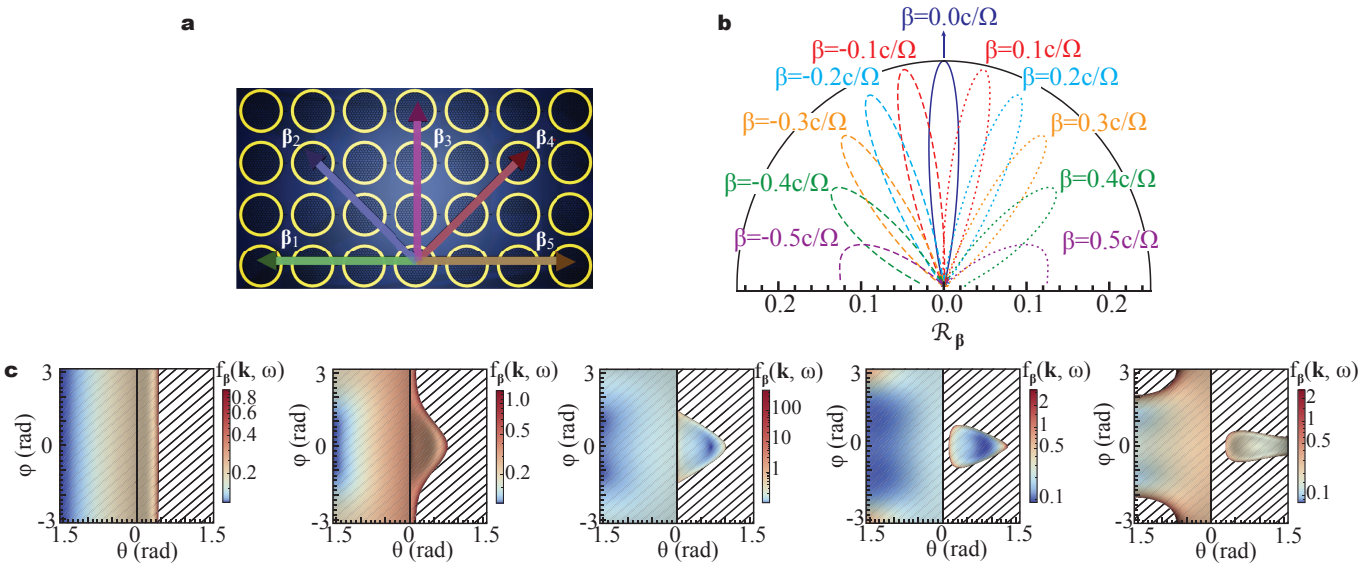

FIG. S3. (a) A linear synthetic phase is imprinted on a metasurface through a traveling-wave modulation and is tuned on demand (colored arrows) to steer the emitted dynamical Casimir photons. (b) Emission lobes of one photon for varying momentum kick and fixed (vertical) emission direction of its twin. (c) Density polar plots of angular emission spectrum for various $\beta = (0, 0.2, 0.3, 0.38, 0.5)\Omega/c$ from left to right. The areas to the right (left) of the vertical solid line correspond to the angular emission spectrum of the high- (low-) frequency photon in a pair. Frequencies are $\omega/\Omega = 0.7$ and $\omega'/\Omega = 0.3$. Shaded zones correspond to forbidden photon emission directions. Between the two rightmost panels two special events simultaneously happen: the merge of the emission "island" of the high-frequency photon with the grazing line and the birth of forbidden regions for the low-frequency photon.

photon. As the magnitude of the momentum kick β increases, the distributions undergo intricate changes. The region of allowed emission for the first photon gets deformed when the kick is non-zero and at a critical value of the kick an "island" of emission appears surrounded by a sea of forbidden emission directions (shaded areas). The island drifts to higher polar angles until it touches the grazing emission line, starts to shrink in size, and finally at $\beta_{max} = \Omega/c$ it collapses to a point and the photon is only emitted parallel to the kick. Far-field emission above that value of the kick is not possible. Regarding the second photon, its emission distribution remains mostly unperturbed until two areas of forbidden emission appear at large polar angles and opposite to the kick direction. The forbidden region grows until it engulfs its allowed emission region and a second island forms (not shown). Finally, it ends up being emitted at a grazing angle but in a direction anti-parallel to the kick. Critical events occur at: (a) $c\beta = \Omega - \omega$: an "island" of emission for the high-frequency photon appears surrounded by a sea of forbidden emission directions; (b) $c\beta = 2\omega - \Omega$: the island touches the grazing emission line; (c) $c\beta = \Omega - 2\omega'$: two areas of forbidden emission for the low-frequency photon appear at large polar angles and opposite to the kick direction; (d) $c\beta = \Omega - \omega'$: an island of emission for the low-frequency photon appears; and (e) $c\beta = \Omega$: both islands collapse and the high- (low-) frequency photon is only emitted parallel (anti-parallel) to the kick. Finally, we. mention that the modulation also excites hybrid entangled pairs composed of one photon and one evanescent surface wave (shaded areas), and when $\beta > \beta_{max}$ only evanescent modes are created and subsequently decay via non-radiative loss mechanisms.

The spectral weight function is

$$f_\beta(\omega) = u\int_{\theta_{min}(u,b)}^{\theta_{max}(u,b)} d\theta \sin\theta \int_0^{\phi_{max}(\theta,u,b)} d\phi \frac{(b\cos\phi - u\sin\theta)^2\left[u^2(1-u)^2 + \kappa_{1z}^2\kappa_{2z}^2\right] + b^2\sin^2\phi\left[(1-u)^2\kappa_{1z}^2 + u^2\kappa_{2z}^2\right]}{\kappa_{2z}\left[b^2 + u^2\sin^2\theta - 2ub\sin\theta\cos\phi\right]}. \tag{S32}$$

Note that it depends only on the magnitude of the kick and not on its direction because the meta-atoms are rotationally-invariant. Here, $u = \omega/\Omega$, $b = c\beta/\Omega$, $\kappa_{1z}^2 = u^2\cos^2\theta$, and $\kappa_{2z}^2 = (1-u)^2 - b^2 - u^2\sin^2\theta + 2ub\sin\theta\cos\phi$. The propagative condition $\kappa_{2z}^2 > 0$ imposes constraints on the angular integration: $\phi_{max}(\theta, u, b) = \Theta(\theta - \theta^*)\mathrm{Re}\arccos[(u^2\sin^2\theta + b^2 - (1-u)^2)/2ub\sin\theta)] + \Theta(\theta^* - \theta)\pi$, $\theta_{min}(u, b) = \Theta(u+b-1)\mathrm{Re}\arcsin[(u+b-1)/u)]$, and $\theta_{max}(u, b) = \mathrm{Re}\arcsin[(1+b-u)/u)]$. Here, $\theta^*(u, b) = \Theta(1-b-u)\mathrm{Re}\arcsin[(1-b-u)/u]$ and $\Theta(x)$ is the Heaviside function. For $b = 0$ we get the spectral weight function for null synthetic phase

$$f_{\Phi=0}(u) = f_{b=0}(u) = -\frac{\pi}{2}u^2(1-u)^2\log|1-2u| + \frac{\pi}{16}(1-2u)^2\log|1-2u| + \frac{\pi}{8}u(1-u)(u^2 + (1-u)^2) \tag{S33}$$

that has a logarithmic divergency at $u = 1/2$ due to emission of twin photons. For $b \neq 0$ there is no simple analytical expression for the spectral weight function.

For a high-Q resonance we use $\delta(u - u_{res}) = \lim_{\epsilon\to 0}(16/5\pi)\epsilon^7[(u - u_{res})^2 + \epsilon^2]^{-4}$ and Eq. (S28) to approximate

$$|\Delta\alpha(\Omega u)+\Delta\alpha(\Omega(1-u))|^2 \approx |\Delta\alpha(\Omega u)|^2+|\Delta\alpha(\Omega(1-u))|^2 \approx \frac{5\pi^7 a_1^4\xi_1^2 D^6}{2(512)^2}\Big(\frac{\Delta E_F}{E_F}\Big)^2\Big(\frac{\Omega}{\gamma}\Big)^3 u_{res}^4[\delta(u-u_{res})+\delta(1-u-u_{res})]$$

and the total rate is

$$\Gamma_\beta = \frac{8An_{MS}^2\Omega^5}{512(2\pi)^3c^4}\int_0^1 du\ |\Delta\alpha(\Omega u) + \Delta\alpha(\Omega(1-u))|^2 f_b(u) \approx g\Omega\ (An_{MS}^2 D^6\omega_{res}^4/c^4) f_{b;res}\Big(\frac{\Delta E_F}{E_F}\Big)^2\Big(\frac{\Omega}{\gamma}\Big)^3, \quad \text{(S34)}$$

where we summed over polarizations and considered a free-standing metasurface, which together bring a factor of $2 \times 2 \times 2 = 8$ (two polarizations, two emissions directions along z for one photon and two emission directions for the other photon). Here, $g = 5\pi^4 a_1^4\xi_1^2/2(512)^3$ and $f_{b;res} = f_b(\omega_{res}, \Omega)$. Note that when $b = 0$ a resonance at $u_{res} = 1/2$ is singular because the delta approximation is right at the divergency of $f_{b=0}(u)$ and Eq.(S34) cannot be used. The same procedure holds for an arbitrary synthetic phase.

Numerically we find that $f_{b\neq 0}(u)$ has a sharp feature at $u = (1 - b)/2$, corresponding to the sudden birth of forbidden regions for the low-frequency photon when $\theta^*(u, b) = \pi/2$ (left side of rightmost panel in Supplementary Figure 3c). An identical feature symmetrically appears at $u = (1 + b)/2$ when the island of emission of the high-frequency photon touches the grazing line $\theta_{max}(u, b) = \pi/2$ (between the two rightmost panels in Supplementary Figure 3c). The functions $\theta^*(u, b)$ and $\theta_{max}(u, b)$ have infinite jumps in their derivatives at the respective points: $\lim_{u\to[(1-b)/2]^-} \partial_u\theta^*(u, b) \to \infty$, $\lim_{u\to[(1-b)/2]^+} \partial_u\theta^*(u, b) = 0$; and $\lim_{u\to[(1+b)/2]^+} \partial_u\theta_{max}(u, b) \to \infty$, $\lim_{u\to[(1+b)/2]^-} \partial_u\theta_{max}(u, b) = 0$. These discontinuities are responsible for the observed sharp edges of the plateaus in Fig. 4a of the main text.

VII. TWO-PHOTON EMISSION FROM STQMS WITH SPINNING SYNTHETIC PHASE

We employ non-paraxial quantization of the electromagnetic field with angular momentum using vector-Bessel (VB) modes [13]

$$\mathbf{A}^{(VB)}_{k,k_z,m,s_t=\pm}(\rho,\varphi,z) = \frac{e^{im\varphi}e^{ik_z z}}{4\pi\omega}\left[(ck_z \mp \omega)J_{m+1}(k\rho)\frac{-i\mathbf{x}-\mathbf{y}}{\sqrt{2}} + (ck_z \pm \omega)J_{m-1}(k\rho)\frac{i\mathbf{x}-\mathbf{y}}{\sqrt{2}} + ck_z J_m(k\rho)\mathbf{z}\right], \quad \text{(S35)}$$

where $J_m(x)$ are Bessel functions. VB modes are eigenstates of the transverse and axial linear momenta, as well as of the total angular momentum (OAM+spin) and transverse spin angular momentum, with eigenvalues $\hbar k$, $\hbar k_z$, $\hbar m$, and $s_t = \pm\hbar c k_z/\omega$, respectively. The dispersion relation is $\omega^2/c^2 = k^2 + k_z^2$ and does not depend on the angular momentum index m nor on s_t. We use first-order time-dependent perturbation theory to compute two-photon generation rates and obtain energy and angular momentum conservation relations $\omega + \omega' = \Omega$ and $m + m' = \ell$. The expectation value of the Poynting vector $\langle\mathbf{S}\rangle = \mu_0^{-1}\langle\mathbf{E}\times\mathbf{B}\rangle$ on the evolved two-photon quantum state has a single vortex singularity along the $z-$axis for $\ell \neq 0$ and a $2\pi\ell$ phase-wrapping around the vortex. The angular momentum decomposition of the spectral weight function is

$$f_\ell(\omega) = \sum_m f_\ell(m, \omega), \quad \text{(S36)}$$

$$f_\ell(m,u) = \pi\int_0^u \frac{\kappa d\kappa}{\kappa_z}\int_0^{1-u}\frac{\kappa' d\kappa'}{\kappa'_z}\mathcal{R}^2\mathcal{I}^{(\mathcal{R})}_{m,\ell}\Big\{[2u^2-\kappa^2][2(1-u)^2-(\kappa')^2]\ \mathcal{I}^{(\mathcal{R})}_{m,\ell} + \kappa^2(\kappa')^2\ \mathcal{I}^{(\mathcal{R})}_{m-2,\ell}\Big\} = f_\ell(\ell-m, 1-u),$$

where $f_\ell(m, \omega)$ is the angular-momentum spectrum. Here, $u = \omega/\Omega$, $\mathcal{R} = R\Omega/c$ with R the radius of the metasurface, and $\mathcal{I}^{(\mathcal{R})}_{m,\ell}(\kappa,\kappa') = \int_0^1 d\eta\ \eta J_m(\kappa\eta\mathcal{R})J_{m-\ell}(\kappa'\eta\mathcal{R})$. The total photo-emission rate is

$$\Gamma_\ell = \frac{An_{MS}^2\Omega^5}{512\pi^3c^4}\int_0^1 du\ |\Delta\alpha(\Omega u) + \Delta\alpha(\Omega(1-u))|^2 f_\ell(u) \approx g\Omega u_{res}^{10}\sum_m f_\ell(m, u_{res}). \quad \text{(S37)}$$

For $\ell = 0$, $\mathcal{I}^{(\mathcal{R})}_{m,0}(\kappa,\kappa')$ is one of Lommel's integrals and has a closed form for all values of $\mathcal{R}$, and for $\mathcal{R} \gg 1$ we approximate $\mathcal{R}^2\mathcal{I}^{(\mathcal{R})}_{m,0}(\kappa,\kappa') \approx \int_0^\infty dx\ xJ_m(\kappa x)J_m(\kappa' x) = \delta(\kappa-\kappa')/\kappa$. Thus,

$$f_{\ell=0}(m,u) \approx \frac{\pi}{2}\int_0^{\min[u,1-u]} d\kappa\ \kappa\ [J_m^2(\kappa\mathcal{R}) - J_{m-1}(\kappa\mathcal{R})J_{m+1}(\kappa\mathcal{R})]\frac{(2u^2-\kappa^2)(2(1-u)^2-\kappa^2)+\kappa^4}{\sqrt{u^2-\kappa^2}\sqrt{(1-u)^2-\kappa^2}}. \quad \text{(S38)}$$

We use $\sum_m J_m^2(x) = 1$ and $\sum_m J_{m-1}(x)J_{m+1}(x) = 0$ to sum over angular momenta to get the spectral weight function. We recover the spectral weight function and emission rate for null synthetic phase, $f_{\ell=0}(\omega) = f_{\beta=0}(\omega) = f_{\Phi=0}(\omega)$ and $\Gamma_{\ell=0} = \Gamma_{\beta=0} = \Gamma_{\Phi=0} \approx g\Omega u_{res}^{10} f_{\Phi=0}(u_{res})$. In the limit $\mathcal{R} \to \infty$ Eq. (S38) vanishes, implying that the summation over m and the infinite metasurface limit do not commute. For other values of ℓ the integral $\mathcal{I}_{m,\ell}^{(\mathcal{R})}(\kappa, \kappa')$ does not have a closed form and must be computed numerically.

[1] A. B. Evlyukhin, C. Reinhardt, E. Evlyukhin, and B. N. Chichkov, Multipole analysis of light scattering by arbitrary-shaped nanoparticles on a plane surface, J. Opt. Soc. Am. B **30**, 2589 (2013).

[2] X. Guo, Y. Ding, Y. Duan, and X. Ni, Nonreciprocal metasurface with space-time phase modulation, Light: Science & Applications **8**, 123 (2019).

[3] H. J. Eichler, P. Günter, and D. H. Pohl, *Laser induced dynamical gratings* (Springer-Verlag, Heidelberg, 1986).

[4] D. Naidoo, K. Ait-Ameur, M. Brunel, and A. Forbes, Intra-cavity generation of superpositions of Laguerre-Gaussian beams, Appl. Phys. B, **106**, 683-690 (2012).

[5] G. F. Calvo, A. Picón, and E. Bagan, Quantum field theory of photons with orbital angular momentum, Phys. Rev. A **73**, 013805 (2006).

[6] P. Rungta, V. Buzek, C. M. Caves, M. Hillery, and G. J. Milburn, Universal state inversion and concurrence in arbitrary dimensions, Phys. Rev. A **64**, 042315 (2001).

[7] F. Mintert, A. R. R. Carvalho, M. Kuś, and A. Buchleitner, Measures and dynamics of entangled states, Phys. Reports **415**, 207-259 (2005).

[8] J. L. Cheng, N. Vermeulen and J. E. Sipe, Third-order nonlinearity of graphene: Effects of phenomenological relaxation and finite temperature, Phys. Rev. B **91**, 235320 (2015).

[9] S. A. Mikhailov, Quantum theory of the third-order nonlinear electrodynamic effects of graphene, Phys. Rev. B **93**, 085403 (2016).

[10] R. Yu, J. D. Cox, J. R. M. Saavedra, and F. J. García de Abajo, Analytical modeling of graphene plasmons, ACS Photonics **4**, 3106 (2017).

[11] Y. Muniz, A. Manjavacas, C. Farina, D. A. R. Dalvit, and W. J. M. Kort-Kamp, Two-Photon Spontaneous Emission in Atomically Thin Plasmonic Nanostructures, Phys. Rev. Lett. **125**, 033601 (2020).

[12] C. L. Holloway, M. A. Mohamed, E. F. Kuester, and A. Dienstfrey, Reflection and transmission properties of a metafilm: with an application to a controllable surface composed of resonant particles, IEEE Transactions on Electromagnetic Compatibility **47**, 853-865 (2005).

[13] S. J. Van Enk and G. Nienhuis, Commutation rules and eigenvalues of spin and orbital angular momentum of radiation fields, J. Mod. Opt. **41**, 963-977 (1994).